Die approbierte Originalversion dieser Diplom-/Masterarbeit ist in der Hauptbibliothek der Technischen Universität Wien aufgestellt und zugänglich.
http://www.ub.tuwien.ac.at

The approved original version of this diploma or master thesis is available at the main library of the Vienna University of Technology.
http://www.ub.tuwien.ac.at/eng

Univ.Prof. Friedrich Aumayr

TECHNISCHE
UNIVERSITÄT
WIEN
Vienna | Austria

DIPLOMARBEIT

Divertor and pedestal dynamics in between edge localized modes at ASDEX Upgrade

Ausgeführt am
Institut für Angewandte Physik
der Technischen Universität Wien
und
Max-Planck-Institut für Plasmaphysik
in Garching

unter der Anleitung von
Univ.Prof. Dr. Friedrich Aumayr
Univ.Doz. Dr. Elisabeth Wolfrum
Dipl.-Ing. Florian Laggner

durch
Sebastian Keerl
Matrikelnummer 0707502
Barnabitengasse 4/1/8, A-1060 Wien

Wien, 10. Mai 2016

Sebastian Keerl

Abstract

Future fusion devices like ITER and DEMO will be operated in the high confinement mode (H-mode). The H-mode is characterized by high pressure, temperature and density gradients in the plasma edge due to an edge transport barrier, and therefore high pressure, temperature and density in the plasma core. However, so called edge localized modes (ELMs) lead to the destruction of the edge transport barrier and particles and heat are expelled onto the plasma facing components, e.g. the vessel wall and the divertor. The post-ELM edge plasma density and temperature evolutions are of major interest as they shed light on the dominant transport processes in the edge transport barrier.

In this thesis the inter-ELM evolution of the edge transport barrier is investigated together with the time-resolved behaviour of outer and inner divertor for different gas puffing rates. It is shown that the low field side inter-ELM evolution of the midplane density and temperature is linked to the outer divertor density and temperature and to midplane fluctuations at the plasma edge. A clear link between the outer and inner divertor inter-ELM evolution cannot be identified. The simultaneous examination of the inter-ELM evolution of the midplane edge profiles, outer divertor profiles and midplane fluctuations leads to a model wherein the density recovery rate can be seen as a result of an interplay between a local ionization source, due to incoming neutrals originating from the chamber wall, and the outward particle flux, due to particle transport caused by fluctuations seen as magnetic oscillations. The transient density increase at the outer divertor due to an ELM can be followed by a second density rise. The mechanism of this phenomenon can be explained through the occurrence of midplane fluctuations. The ionization source, due to incoming neutrals, which are recycled from plasma facing components, increases after an ELM event and is modelled using a one dimensional transport algorithm KN1D. This transport algorithm and the continuity equation, assuming a drift–diffusion model, lead to the estimation of additional particle transport, that originates from midplane fluctuations, of the order of $1\,\frac{\mathrm{m}^2}{\mathrm{s}}$.

Zusammenfassung

Zukünfitge Kernfusionsanlagen wie ITER und DEMO sollen in der H-mode (high confinement mode) betrieben werden. Dieser Betriebsmodus zeichnet sich durch hohe Druck-, Temperatur- und Dichtegadienten am Plasmarand aufgrund des Auftretens der Randtransportbarriere (ETB) aus. Dies führt wiederum zu erhöhtem Druck, Temperatur und Dichte im Inneren des Plasmas. Jedoch treten in diesem Betriebsmodus sogenannte ELMs (edge localized modes) auf, die zur Zerstörung der ETB und dadurch zu flachen Gradienten am Plasmarand führen. Dies hat zur Folge, dass Teilchen aus dem Plasmarand auf die Gefäßwand und die Divertoren fliegen. Das Verständnis der darauf folgenden Entwicklung bis zur Wiederherstellung der ETB ist von großer Bedeutung, da diese Einsicht in die dominanten Transportprozesse in der ETB gibt.

Im Rahmen dieser Arbeit wurde die ETB und das zeitaufgelöste Verhalten des inneren und äußeren Divertors bei unterschiedlichen Deuterium Neutralgasraten untersucht. Dabei konnte gezeigt werden, dass die Entwicklung der Elektronendichte und -temperatur an der Mittelebene nach dem ELM mit der Dichte- und Temperaturentwicklung am äußeren Divertor und mit Fluktuationen an der Mittelebene zusammenhängt. Eine deutliche Korrelation zwischen der Dichte- und Temperaturentwicklung des äußeren und inneren Divertors ist nicht zu erkennen.

Die simultane, ELM synchronisierte Betrachtung der Mittelebe, des äußeren Divertors und der Fluktuationen führen zu einem Modell, bei dem die Rate des Dichteanstiegs an der Mittelebene als Balance des Zwischenspiels von Teilchenausstoß durch magnetische Turbulenzen und einer lokalen Ionisationsquelle innerhalb der Separatrix gesehen werden kann. Dabei kann der zweite Elektronendichteanstieg am äußeren Divertor durch das Auftreten von Fluktuationen an der Mittelebene in dieser Arbeit erklärt werden. Die Ionisationsquelle, die von Teilchen herrührt, die aufgrund von Recycling an der Gefäßwand auftreten, steigt nach dem ELM an und kann mit dem KN1D Code modelliert werden. Abschließend führt diese Modellierung zusammen mit der Kontinuitätsgleichung, welche auf dem Drift-Diffusions-Modell basiert, zu einer Abschätzung des von Fluktuationen stammenden, zusätzlichen Teilchentransports in der Größenordnung von $1\,\frac{\mathrm{m}^2}{\mathrm{s}}$.

Contents

Abstract **i**

Zusammenfassung **iii**

1 Introduction **1**
- 1.1 Nuclear Fusion . . . 1
  - 1.1.1 Why Nuclear Fusion? . . . 1
  - 1.1.2 How could Nuclear Fusion work? . . . 2
- 1.2 High confinement mode and edge localized modes . . . 8
- 1.3 Objectives of this thesis . . . 10

2 Review of the inter-ELM phase **11**
- 2.1 Inter-ELM phase at the outer midplane . . . 11
- 2.2 Inter-ELM phase at the outer divertor . . . 13
- 2.3 Magnetic oscillations in the inter-ELM phase . . . 16

3 Used diagnostics and data analysis **21**
- 3.1 Midplane diagnostics . . . 21
  - 3.1.1 Lithium beam impact excitation spectroscopy . . . 21
  - 3.1.2 Electron cyclotron emission measurement . . . 23
  - 3.1.3 Thomson scattering diagnostic . . . 24
  - 3.1.4 Deuterium cyanide laser interferometry . . . 25
  - 3.1.5 Integrated data analysis . . . 26
  - 3.1.6 Pick up coil measurements . . . 28
- 3.2 Divertor region diagnostic . . . 28
  - 3.2.1 Stark broadening diagnostic . . . 28
- 3.3 Divertor target diagnostic . . . 29
  - 3.3.1 Langmuir probes . . . 29

4 Experimental investigation of the inter-ELM phase **33**
- 4.1 Influence of the deuterium fuelling rate . . . 33
  - 4.1.1 Outer midplane . . . 33
  - 4.1.2 Inner and outer divertor . . . 35
  - 4.1.3 Midplane fluctuations . . . 40
- 4.2 Midplane profiles, midplane fluctuations and divertor relation at the low magnetic field side . . . 42

5 Discussion **45**
- 5.1 Interpretation of the low magnetic field side inter-ELM relation . . . 45
- 5.2 Additional flux estimation due to midplane fluctuations by using the continuity equation . . . 46
- 5.3 Comparison of the obtained results with previous investigations . . . 50

6 Summary **51**
6.1 Main results 51
6.2 Future perspectives 52

A Acknowledgement **53**

B List of Figures **55**

C Bibliography **59**

1 Introduction

Nuclear fusion is a promising technology, that together with renewable energies could lead to a carbon free emission energy supply. Chapter 1.1 of this thesis enlightens the advantages of nuclear fusion and the basic ideas of how nuclear fusion could be made possible. Furthermore, chapter 1.2 describes the high confinement mode, the preferred operating condition of nuclear fusion tokamak devices, and edge localized modes, a characteristic phenomenon of the high confinement mode.

1.1 Nuclear Fusion

As the basic concept of nuclear fusion is not widespread among our society, it is important to present advantages of this technology in comparison to nuclear fission, fossil fuel based and renewable energy technologies. After this juxtaposition in chapter 1.1.1, the basic ideas of nuclear fusion will be highlighted in chapter 1.1.2.

1.1.1 Why Nuclear Fusion?

The supply of energy and the increase in energy demands are major issues facing mankind now and will be increasingly critical in the future. With approximately 78% of our current energy supply fossil fuel based [1], there is an accelerated increase in the greenhouse effect due to the rising CO_2 content in the atmosphere, and therefore an accelerated increase in the global temperature. This temperature rise will transform the ecological and environmental equilibrium in a way, that is hardly predictable. Therefore it is of major importance to decelerate the human-induced climate change. Figure 1 shows four represantitve concentration pathways (RCP), each based on a multi-model approach, predicting the global surface air temperature for different CO_2 emission progressions.

On the one hand mankind's energy demand needs to be reduced, on the other hand it is urgent to cut down the amount of CO_2 emission. Renewable energy technologies as for instance solar- and wind power are such carbon free emission technologies. However, those are not able to supply energy at a constant level due to dependency on insolation and wind force, respectively. Hence it is crucial to develop carbon free technologies that can provide energy at a constant level.

One approach to provide such energy could be to expand the provision of energy by nuclear fission, however this leads to a variety of major issues. Among other problems, nuclear waste requires longterm safe storage, as the half-life of ${}^{99}_{43}\mathrm{Tc}$ for example is 211 100 years [3]. Furthermore, nuclear fission runs the risk of nuclear disasters, as seen at *Fukushima Daiichi*.

Considering these disadvantages, alternatively nuclear fusion could play an important role in the future as it provides energy at a steady level, does not have deep geological repository issues, has a vanishingly low risk of leaking of radioactive materials and finally uses resources that are assured for a long time (3000 years counting known Li reserves in the earth, 60 million years counting Li in seawater and 150 billion years counting D reserves at an annual electricity need of the one in 1995 [4]). These advantages of nuclear fusion over other technologies arouse interest of the role nuclear fusion could play in the future.

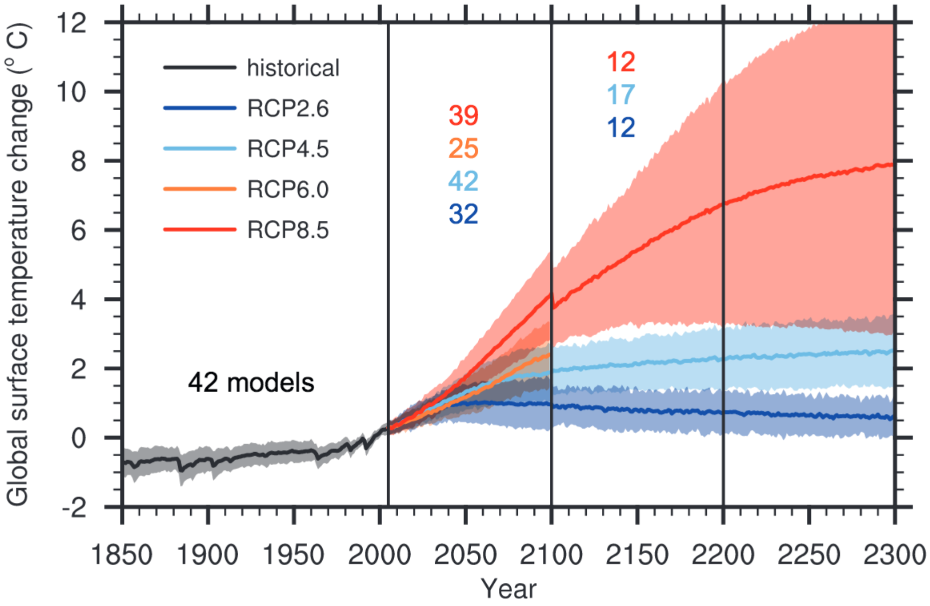

Figure 1: Time series (1850-2300) of global annual mean surface air temperature changes (taken from the *Coupled Model Intercomparison Project Phase 5* concentration-driven experiments). Projections are shown for four *representative concentration pathways* (RCP) for the multi-model mean (solid lines) and ±1.64 standard deviation (5 to 95%) across the distribution of individual models (shading), based on annual means. This shows that according to four different CO_2 emission progressions, the global surface temperature can reach levels of 1 °C, 2 °C, 2.5 °C, 4 °C by the end of the century in addition to the global temperature nowerdays [2].

1.1.2 How could Nuclear Fusion work?

Figure 2 shows the binding energy per nucleon $\frac{B}{A}$ over the nucleon number A. It shows iron $^{56}_{26}$Fe to be the most stable element, with those to either side with a lower binding energy. Due to this fact, nuclear transformation, which results in nuclei closer to $^{56}_{26}$Fe than the original nuclei, converts mass, due to the mass defect, to energy, according to Einstein's law $E = \Delta mc^2$. While nuclear fission follows the concept of neutron induced splitting of high atomic mass nuclei like uranium $^{235}_{92}$U, nuclear fusion works on the principle of combining low atomic mass nuclei.
Figure 2 shows that there are several fusion reactions possible. Some of them are shown in the following:

$$p + p \Rightarrow {}^2_1\mathrm{D} + e^+ + \nu_e + 0.42\,\mathrm{MeV} \tag{1}$$

$${}^2_1D + {}^3_1T \Rightarrow {}^4_2\mathrm{He} + n + 17.6\,\mathrm{MeV} \tag{2}$$

$${}^2_1D + {}^2_1D \Rightarrow \begin{cases} {}^3_2\mathrm{He} + n + 3.3\,\mathrm{MeV} & (50\%) \\ {}^3_1\mathrm{T} + p + 4.0\,\mathrm{MeV} & (50\%) \end{cases} \tag{3}$$

$${}^2_1D + {}^3\mathrm{He} \Rightarrow {}^4\mathrm{He} + p + 18.3\,\mathrm{MeV} \tag{4}$$

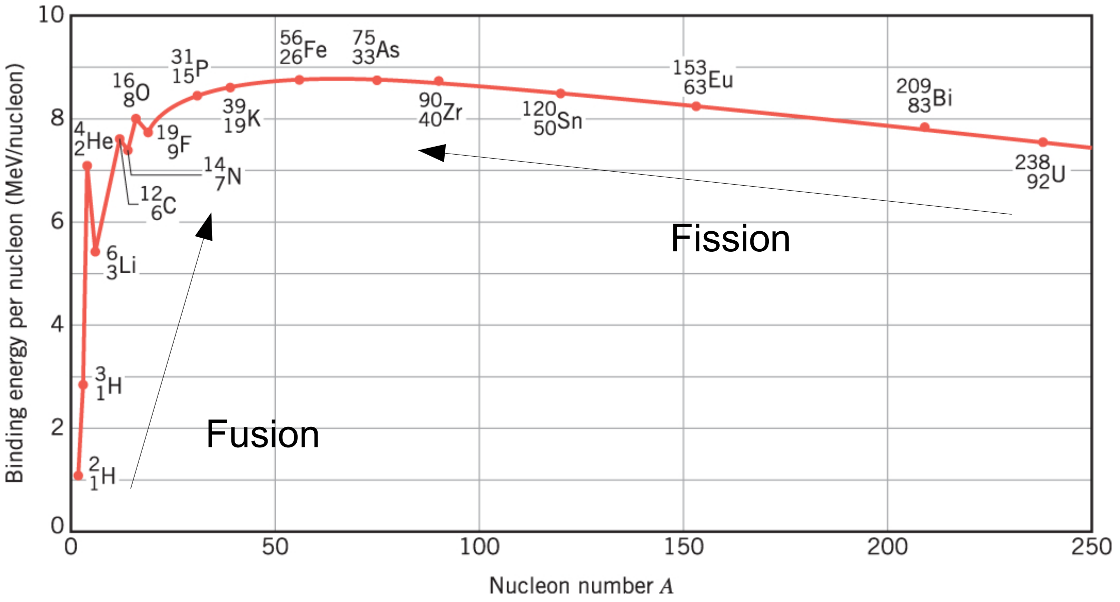

Figure 2: Binding energy per nucleon $\frac{B}{A}$ over nucleon number A [5].

Reaction 1 denotes the proton-proton fusion, resulting in deuterium $^{2}_{1}$D, a positron e^{+}, an electron neutrino ν_e and energy through a β^{+} decay. Reaction 2 denotes the deuterium-tritium fusion to $^{4}_{2}$He, a neutron n and an energy gain of 17.6 MeV. The deuterium-deuterium reaction 3 results with a probability of 50% in $^{3}_{2}$He, a neutron and energy and a probability of 50% in tritium $^{3}_{1}$T, a proton and energy. Reaction 4 denotes the fusion of $^{2}_{1}D$ and ^{3}He to ^{4}He, a proton and an energy gain of 18.3 MeV.

These reactions among others continuously take place in the sun. Their following processes, e.g. electron-positron annihilation, are responsible for the electromagnetic waves (light) that reach earth. This light can be transformed and stored in chemical energy due to the process of photosynthesis. Thus these fusion processes are the engine of all life on earth.

In order to realize nuclear fusion on our planet, it is necessary to find the most effective reaction and hence requires a closer look at the cross sections of the fusing particles, see figure 3. The highest cross section can be achieved by the deuterium tritium (DT) reaction, which peaks around the deuterium energy of approximately 100 keV ($\approx$ 1160 million K).

This cross section represents the fusion probability of deuterium and Tritium and is dependant on their kinetic energy. If the kinetic energy is sufficiently high, the proton consisting particles can come close enough so that the repelling electromagnetic force is overpowered by the attracting strong nuclear force, which is stronger by a factor of about 100 beneath lengths of around 10^{-15} m.

There are three fusion determining variables, whose product (so called fusion product) must exceed a certain value to achieve ignition: density, temperature and the confinement time.

$$n T \tau \geqslant 3 \cdot 10^{21} \, \frac{\mathrm{keVs}}{\mathrm{m}^3} \tag{5}$$

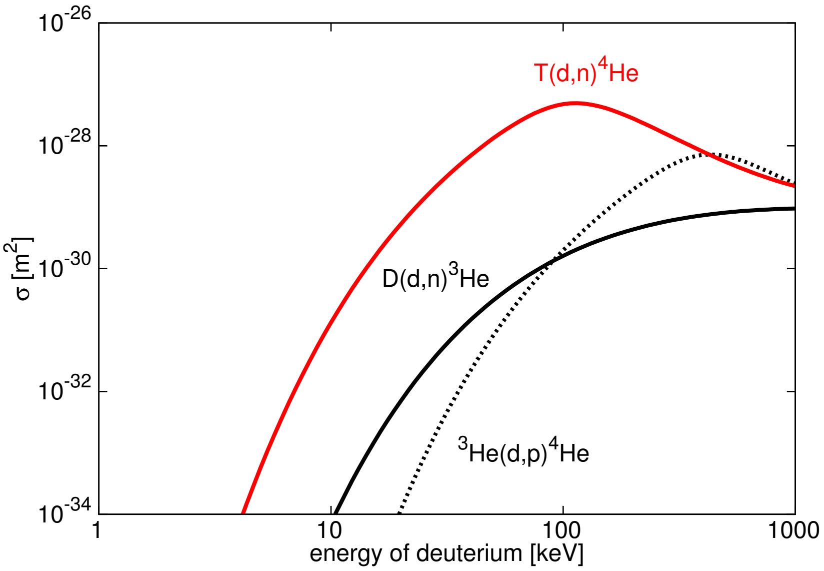

Figure 3: Cross sections for several fusion reactions versus the energy of deuterium. The D-T fusion reaction (T(d,n)^{4}He) has a significantly higher cross section at lower energies than the D-D (D(d,n)^{3}He) or the D-^{3}He (^{3}He(d,n)^{4}He) reaction. Figure taken from [6] with data from [7, 8].

An overview of typical magnitudes of those variables can be found in table 1. The density of the charged particles in the sun reach values of $10^{31}\,\frac{1}{\mathrm{m}^3}$ due to the high gravitational force. Since one cannot achieve such high values on earth, it is necessary to achieve temperatures that exceed those of the core of the sun.

	Density $[\frac{1}{m^3}]$	Temperature $[K]$	Confinem. time [s]
Sun core	10^{31}	15 000 000	∞
Inertial confinem.	10^{31}	100 000 000	10^{-11}
Magnetic confinem.	10^{20}	100 000 000	10

Table 1: Overview of density, temperature and confinement time

The two most important approaches to maximize the fusion product are inertial confinement and magnetic confinement fusion. Inertial confinement reaches a higher density by a factor of 10^{11} but a much lower confinement time by a factor of 10^{-11}.

In magnetic confinement fusion, high temperatures (100 keV) are essential. Since no solid state exists that can withhold these loads, a magnetic field must be set up to confine the charged particles.
Magnetic field coils produce magnetic field lines, which force charged particles to

gyrate around them. While it is necessary to build a self-contained vessel in order to guarantee best possible confinement, these coils are set up toroidally to create a toroidal magnetic field, see figure 4a.
Due to the curvature of those magnetic field lines, the magnetic field is not constant ($B(R) \propto \frac{1}{R}$), and the resulting magnetic field gradient $\vec{B}$ leads to a drift

$$\vec{v}_{\nabla B} \propto \frac{\vec{B} \times \nabla \vec{B}}{q\ B^3}, \tag{6}$$

which is inversely proportional to the electric charge q and perpendicular to $\vec{B}$ and $\nabla \vec{B}$. This entails a separation of electrons and ions and thus to an electric field. This electric field again leads to a drift

$$\vec{v}_E = \frac{\vec{E} \times \vec{B}}{B^2}, \tag{7}$$

which is charge independent and as a result moves particles of both charges horizontally out of the vessel. In order to remedy this problem a poloidal magnetic field is necessary, which, in combination with the toroidal field, produces a helical field. Particles following this helical field will be, whilst being on the low magnetic field side, moved away from the centre due to the gradient drift, and then, whilst being on the high magnetic field side, again towards the center. Hence the net drift is abolished.

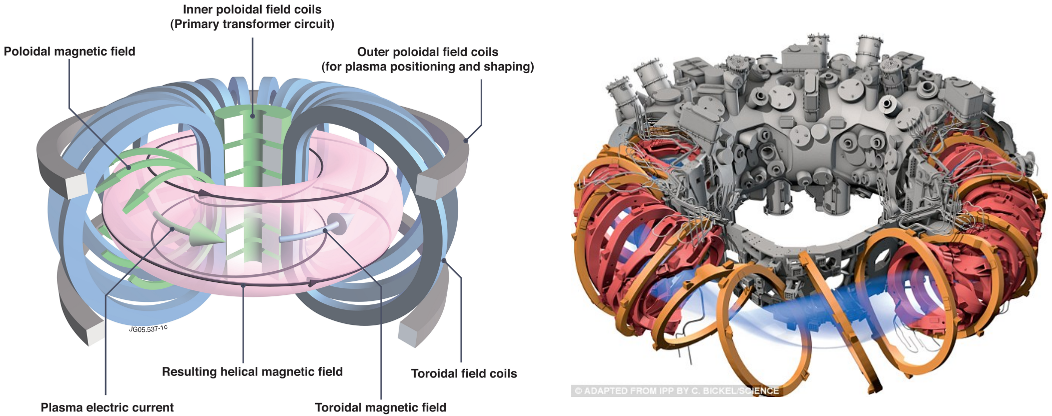
Inner poloidal field coils
(Primary transformer circuit)
Poloidal magnetic field
Outer poloidal field coils
(for plasma positioning and shaping)
JG05.537-1c
Resulting helical magnetic field
Toroidal field coils
Plasma electric current
(secondary transformer circuit)
Toroidal magnetic field
© ADAPTED FROM IPP BY C. BICKEL/SCIENCE

(a) Tokamak concept: arrangement of magnetic field coils and the resulting magnetic field that confines the plasma [9].

(b) Stellarator concept: the helical field is entirely generated through external current-carrying, geometrically twisted coils [10].

Figure 4: Magnetic fusion concepts

The creation of this helical field can be achieved in two different ways leading to two different magnetic confinement fusion concepts, see also figure 4:

- *Tokamak* (from the Russian: toroidal chamber with magnetic coils) concept: an additional inner poloidal field coil can be seen as the primary transformer circuit, the plasma itself as the second electric current. The primary circuit can only be run ramp-like, hence the discharge duration is limited and Tokamaks usually can only be operated in pulsed mode. This induced plasma electric current creates a poloidal magnetic field, which in addition to the toroidal magnetic field results in a helical one.
- *Stellarator* (latin: *stella*, star) concept: the helical field is entirely generated through external current-carrying, geometrically twisted coils. Since there is no plasma current needed, a Stellarator can perform continuous operation.

This thesis was entirely performed at the Tokamak *ASDEX Upgrade* at the *Max Planck Institute of Plasma Physics* in Garching, Germany. *ASDEX Upgrade* plays an important role in the fusion research and is therefore also an influential contributor to *ITER* (latin: the way), a Tokamak fusion experiment at large scale, currently under construction in the south of France [11]. A sketch of how ITER will look like can be seen in figure 5.

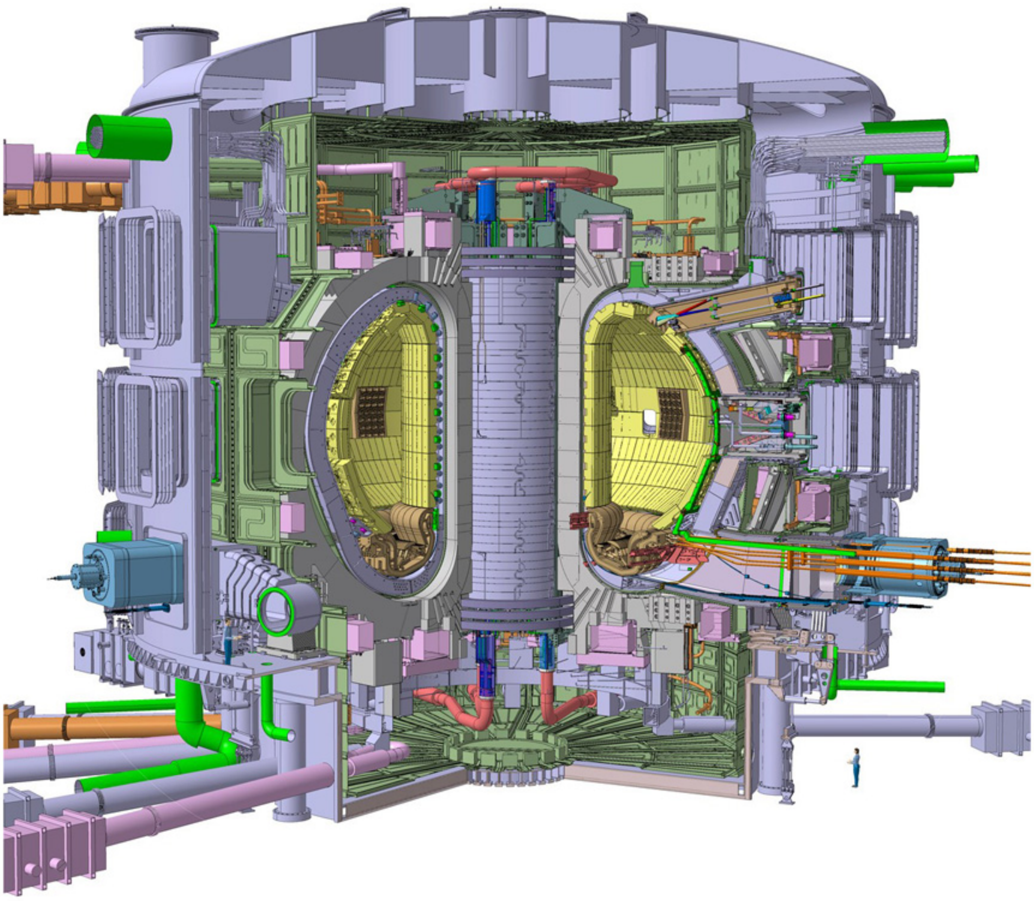

Figure 5: The *ITER* experiment is a Tokomak whose geometry takes its lead from the Garching machine *ASDEX Upgrade* – albeit four times larger (notice the little man to the bottom right)[12].

1.2 High confinement mode and edge localized modes

The magnetic fields, mentioned in chapter 1.1.2, create magnetic flux surfaces, on which charged particles can move along. However, these flux surfaces can be subject to unstable modes leading to turbulent transport. Especially when fusion devices operate in high confinement mode[1] (H-mode) [13], as will be the case with *ITER* and *DEMO*[2] , edge localized modes (ELMs) occur at the plasma edge, resulting in plasma energy loss.

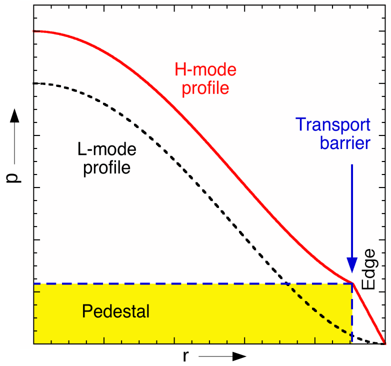

Figure 6: Radial pressure profiles versus minor radius for L-mode (black, dashed) and H-mode (red, solid). In H-mode an edge transport barrier leads to steep edge gradients called the pedestal. [14].

The H-mode (figure 6) is a plasma operating condition of higher ratio of stored kinetic energy versus heating power in contrast to the low confinement mode (L-mode). A radial electric field $\vec{E}_r$, created by the main ion species, respectively the pressure gradient term in the radial force balance, leads to a $\vec{E}_r \times \vec{B}$ velocity shear of charged particles at the plasma edge [15]. This shear suppresses radial transport and consequently produces a region with steep pressure, density and temperature gradients, the so called edge transport barrier (ETB).
As mentioned before, edge localized modes (ELMs) occur in this desired high confinement mode. Figure 7 depicts a typical ELM cycle. A poloidal cross section of a Tokamak vessel is shown in the sketch on the far left. The confined plasma is framed by the separatrix, which is the last closed flux surface (LCF) and the scrape off layer (SOL) lies outside the separatrix. All the flux surfaces within the SOL border on the divertor plates, which can be seen in the poloidal cross section in figure 7. The ELM cycle dynamics of the pressure profile can be found below these poloidal cross sections of figure 7.
At first the plasma is in the quiet phase and the pressure gradient at the edge of the plasma rises. At a certain point the pressure gradient clamps, however, the pedestal width still widens and therefore the pedestal height still builds up [17]. If this pressure gradient reaches a certain value, it can destabilize ballooning modes. At the same time, this pressure gradient drives an additional current, the bootstrap

---

[1] The term 'mode' here refers to an operational type in contrast to a standing wave mode as in edge localized mode

[2] Future fusion device, that will demonstrate the economical capability of nuclear fusion.

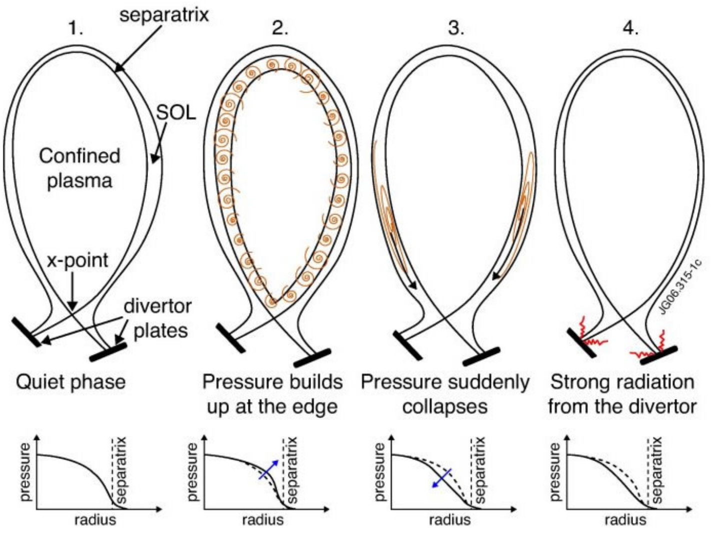
1.
separatrix
2.
3.
4.
SOL
Confined plasma
x-point
divertor plates
JG06.315-1c
Quiet phase
Pressure builds up at the edge
Pressure suddenly collapses
Strong radiation from the divertor
pressure
separatrix
radius

Figure 7: Typical edge localized mode (ELM) cycle in a poloidal cross section and its corresponding pressure profile progression [16].

current, which at a certain threshold destabilizes peeling modes [18, 19]. Figure 8 shows this linkage of the peeling and ballooning mode boundaries and that its trespassing leads to a destabilization and thus to the triggering of an ELM.

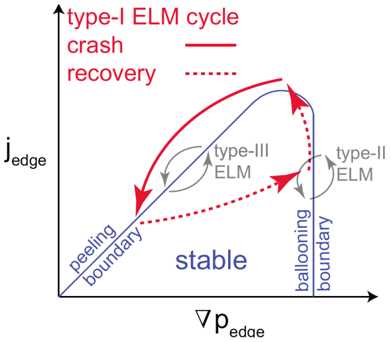
type-I ELM cycle
crash
recovery
j_{edge}
type-III ELM
type-II ELM
peeling boundary
stable
ballooning boundary
∇p_{edge}

Figure 8: Bootstrap current versus pressure gradient. Typical ELM cycles, according to each type, are shown in this peeling-ballooning stability diagram [20].

This leads to a sudden drop in the pressure gradient as well as to convective particle and heat transport into the SOL and onto the plasma facing components (PFC), most of it to the divertor target plates, possibly exceeding their tolerable power load. This results in damage and erosion of the PFCs, releasing impurities to the plasma and hence reduces the energy confinement through increased radiated power. Consequently a profound understanding of ELMs is required to be able to control and eventually mitigate those.

According to the conventional classification, there are three different types of ELMs [21, 22, 23]:

- Type-I ELMs: The red curve in figure 8 shows the cycle of such a type-I

ELM. Its repetition frequency increases with the energy flux P_{sep} through the separatrix into the SOL [21].

- Type-II ELMs: The grey curve to the right of figure 8 indicates that those types live at the ballooning boundary. They mainly occur in plasmas with high triangularity[3], which enlarges the peeling-ballooning mode stability boundary, have a high repetition frequency and a low power loss compared to type-I ELMs [22].
- Type-III ELMs: These ELMs, like type-II ELMs, are smaller than type-I. They occur at the peeling stability boundary and therefore already trigger at low pressure gradients. Their repetition frequency decreases with the energy flux through the separatrix and coherent magnetic precursor oscillations can be observed.

1.3 Objectives of this thesis

As type-I ELMs lead to the destruction of the edge transport barrier (ETB) and thus to the flattening of the plasma edge gradients, the plasma stored energy gets reduced. The recovery to the pre-ELM state evolves in a certain manner. In order to investigate this post-ELM evolution at *ASDEX Upgrade*, following steps have been performed in this thesis:

- Characterization of the ELM synchronized electron density and temperature inter-ELM evolution at the outer and inner divertor, the outer midplane (denoted in figure 15) and radial magnetic field fluctuations, detected at the outer midplane, in the following termed midplane fluctuations.
- Investigation of the deuterium fuelling influence on the inter-ELM evolutions mentioned in the previous bullet point.
- Identification of dependencies between outer midplane, midplane fluctuations and divertor evolution and presentation of a model to explain those relations.
- Quantification of the additional particle transport caused by midplane fluctuations using the drift-diffusion model based continuity equation.

This thesis is structured as follows. Chapter 2 reviews the current status of inter-ELM comprehension of the outer midplane, the outer divertor and the midplane fluctuations at the plasma edge. Furthermore chapter 3 gives an overview of the used diagnostics at the midplane, the divertor region and the divertor target. The experimental investigation in chapter 4, showing the deuterium fuelling dependency, the link between the outer midplane, midplane fluctuations and outer divertor, is followed by chapter 5, which introduces a model that quantifies the inter-ELM particle transport using the drift-diffusion model based continuity equation. Chapter 6 gives a summary and an outlook on possible improvements to this simple model.

---

[3] plasma shape parameter: $\delta = \frac{\delta_{upper}+\delta_{lower}}{2} = (\frac{R_{geom}-R_{upper}}{a} + \frac{R_{geom}-R_{lower}}{a})/2$ [24]

2 Review of the inter-ELM phase

This chapter provides a review of recent investigations into the phase between two ELM crashes, the so-called inter-ELM phase. The inter-ELM phase investigation can be improved by synchronizing data to the ELM onset time, which is also called conditional synchronization. For a number of similar ELMs data points are layered on top of each other relative to the ELM onsets. This provides a powerful tool to investigate ELMs and their intermediate phases at the same time.

Chapter 2.1 reviews investigations into the inter-ELM phase at the outer midplane, see figure 15, significantly exploring the inter-ELM density, temperature and pressure profiles evolution. These steep profiles at the plasma edge flatten due to an ELM event, see bottom sketch of figure 7, and recover again to pre-ELM values at certain rates. This recovery of the profiles in particular is the subject of these investigations. Chapter 2.2 reviews the inter-ELM phase at the divertor, which is thought to be linked to the midplane inter-ELM phase. Opposing explanations for the temporal inter-ELM density evolution are highlighted. Finally, chapter 2.3 describes midplane fluctuations at the low magnetic field side and correlates fluctuation evolutions with pedestal evolutions.

2.1 Inter-ELM phase at the outer midplane

Electron density, temperature, pressure and their gradient profiles at the plasma edge are important plasma parameters, as they determine the plasma core values in H-Mode, see figure 6. However, these profiles flatten with the occurrence of an ELM crash. As this substantially influences plasma core values, the recovery of these profiles is of major interest.

Reference [25] investigates the recovery of the electron density, temperature and pressure profiles at different fuelling levels and medium collisionality at *ASDEX Upgrade*. It shows that the electron density and temperature profile evolution phases are linked. However, the electron density profile recovers faster than the electron temperature profile.

Figure 9 shows the electron temperature gradient and electron density gradient evolution relative to the ELM onset. This evolution can be divided into six distinct phases. Phase I depicts the phase shortly before the ELM crash (phase II). Phase III is characterized by rapid ∇n_e recovery whilst constant ∇T_e. ∇n_e stalls in phase IV, during which ∇T_e continues to recover until its final recovery in phase V. ∇n_e recovers completely before phase V at a fast rate. Phase VI denotes pre-ELM values and is therefore identical with phase I.

The electron pressure p_e can be calculated through n_e and T_e. Its evolution also shows a drop in phase II and a recovery time similar to the one of T_e. According to the peeling-ballooning theory, a high pressure gradient leads to destabilization of the ETB. However, the pressure limit cannot explain the ELM onset on its own. Reference [26] highlights that although the pressure gradient is clamped, the pedestal width continues to grow until the end of the ELM cycle.

Figure 10 shows the operational points at each evolution phase and its associated peeling-ballooning stability boundary. It shows that the operational point from

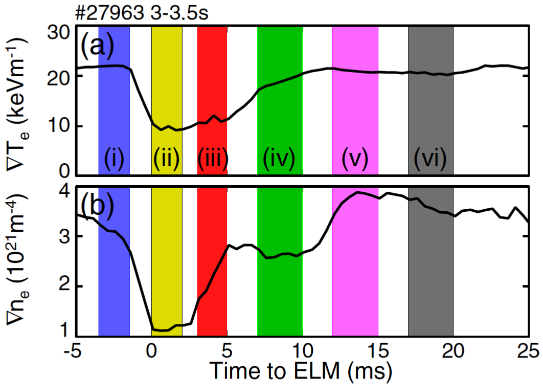

Figure 9: (a) Temperature gradient and (b) density gradient evolution relative to the ELM onset. This evolution is divided into six phases: phase I (blue), phase II (yellow), phase III (red), phase IV (green), phase V (magenta) and phase VI (grey) [26].

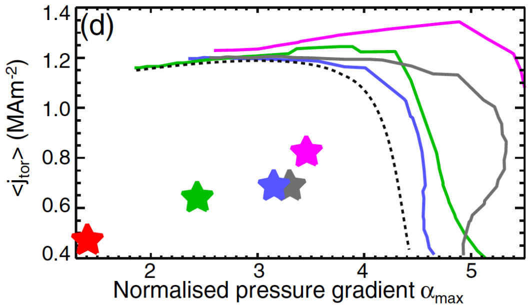

Figure 10: ELM resolved edge current density versus normalized edge pressure gradient. Operational points denoted by stars, peeling-ballooning stability boundaries by curves (color codes as in figure 9) [26].

phase V onwards is fixed. However, the PB boundary moves closer and closer with each phase towards this operational point. More and more poloidal harmonics become unstable in the ETB during the widening of the pedestal width and therefore the stability boundary sets in at lower values. However, the black dashed line in figure 10 denotes the PB boundary at the ELM crash, showing that the operational point is still too far away from the PB boundary. Therefore the final ELM trigger condition cannot be determined by linear MHD stability alone [27].
Reference [25] also shows an increase in the time interval between the ELM crash and the start of the first recovery phase with increasing deuterium fuelling rate. This time interval increase can be correlated to data from the magnetic pick up coils, which indicates turbulence at the plasma edge, suggesting that the start of the recovery coincides with the suppression of the turbulent transport caused by the ELM crash.

With the identification of these different recovery phases, it is of interest to identify the dominant transport type of turbulence in these phases. This question is investigated by [28] in detail by using *GENE* [29] to perform gyrokinetic simulations of the

inter-ELM profile evolution at *ASDEX Upgrade*. It was found that the early density build-up phase transport is dominated by the density gradient driven trapped electron modes (TEM). These can be active due to the weak $\vec{E} \times \vec{B}$ flow shear in this phase. *GENE* modeled diffusion values are in the order of $0.025\,\frac{\mathrm{m}^2}{\mathrm{s}}$. However, at later phases, ∇T_e reaches a critical value concurrent with the appearance of micro-tearing mode (MTM) and electron temperature gradient (ETG) instabilities. Although ETG could be responsible for most of the electron heat flux, the full transport needs a stronger mechanism. Possible candidates for producing additional electron heat flux are MTM or kinetic ballooning mode (KBM) instabilities.
These observations of the ELM induced profile crash and its resulting recovery have also been observed at the *DIII-D* tokamak in *San Diego, USA*. Reference [30] examined n_e, T_e, p_e profiles and the according gradient profiles in order to test *EPED*, a model that is built to predict the pedestal height and width. In doing so, the pedestal profile evolutions also show a drop at the ELM crash with subsequent recovery, whereby the initial, rapid recovery leads to 85% of the pre-ELM values within 20% - 40% of the inter-ELM cycle. *EPED* is based on two hypothesis. First, the maximum pressure is limited by the onset of peeling-ballooning MHD modes and second, the pressure gradient triggers kinetic ballooning modes (KBM) even before the pedestal reaches the PB limit.

2.2 Inter-ELM phase at the outer divertor

The outer divertor, see figure 15, is related to the outer midplane. This relation, as well as the ELM averaged (synchronized) evolution of the electron density and the temperature at the divertor target are under investigation in the following presented references.

Reference [31] describes the dynamics of retention, implantation, desorption and recycling of deuterium at the divertor target at the *Joint European Torus* (JET) tokamak experiment in *Culham, UK*. It shows an increase in the target surface temperature with ongoing plasma exposure.
This and the additional ELM related incident deuteron fluxes and energies change the balance of the above mentioned processes.
A study of the dynamic behaviour on an ELM resolvable timescale revealed a complex interplay of deuterium refuelling and desorption. These investigations reveal that a pronounced second peak in the outer divertor photon flux D_α and outer divertor ion flux D^+ evolution occurs at $\sim 8\,\mathrm{ms}$ after the ELM-onset, see figure 11. This effect exists at the ITER-like wall (Beryllium in the main chamber and tungsten at the divertor) JET experiment, but not at the carbon wall experiment JET-C.
At the same time, the impurity flux or the sputtering flux to the target do not show a second peak. [31] suggests this peak is not related to ions from the pedestal, otherwise a second peak in the impurity flux would be observed. In addition, the impact energy of the second peak flux is below the sputtering threshold of tungsten by deuterium or beryllium. [31] also suggests to explain the coherent appearance of the deuteron flux and the neutral atom radiation through local recycling and the time delay of 8 ms through longer diffusion time due to deep penetration.

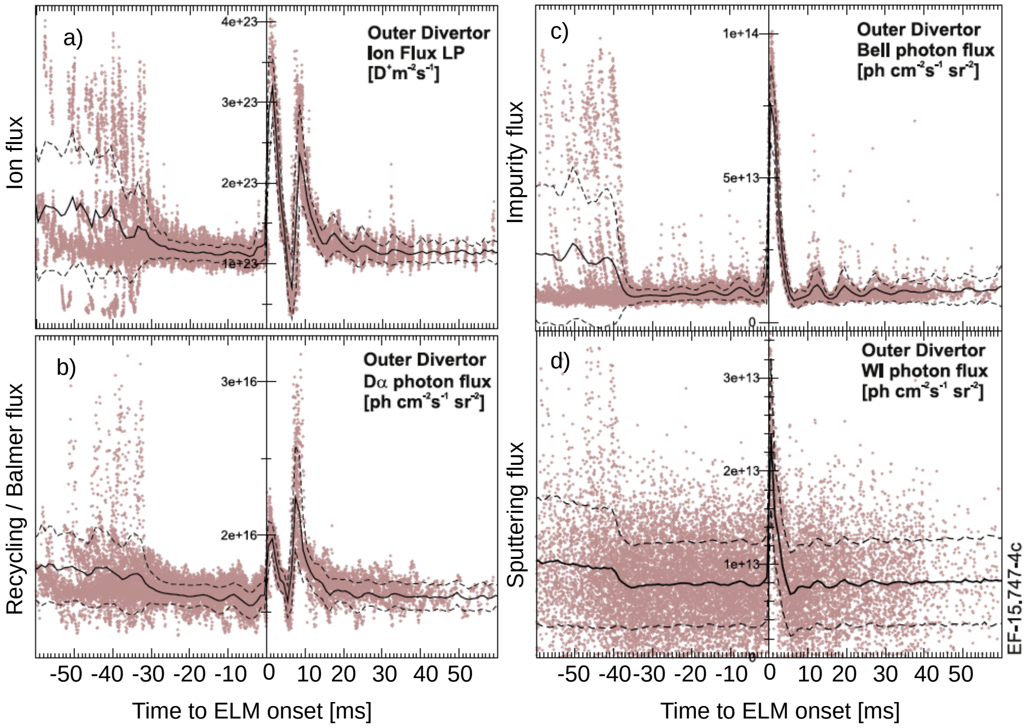

Figure 11: ELM time averaged (a) total impinging ion flux measured by Langmuir Probes, (b) total D_α photon flux as marker for recycling, (c) photon flux resulting from impinging Be ions (BeII at 527.1 nm), and (d) photon flux of sputtered W atoms from the bulk-W divertor PFCs (WI at 400.9 nm) [31].

A model to simulate an H-Mode discharge with type-I ELMs at the *DIII-D* tokamak is given by [32]. This UEDGE-MB model incorporates the macro-blob model, which describes an ELM as a combination of several macro-blobs. Furthermore it describes the temporal evolution of the pedestal plasma profiles, the divertor recycling and the wall inventory. A closer look at ELM resolved evolutions is presented. 2.7 ms after an ELM crash, cold ($T_e \approx 10\,\mathrm{eV}$) and dense ($n_e \approx 6 \times 10^{19}\,\frac{1}{\mathrm{m}^3}$) plasma evolves at the outer divertor target. This dense plasma is opaque to neutrals, therefore no fuelling of the pedestal from the divertor takes place. At the same time high radial plasma transport ($D \approx 1\,\frac{\mathrm{m}^2}{\mathrm{s}}$) leads to a pedestal inventory decrease and divertor plasma increase. 3 ms after the ELM crash, the transport barrier is restored, therefore neutrals penetrating through the separatrix will be ionized in the plasma and are well confined. This leads to a decrease in the heat flux into the SOL and thus to a drop in the divertor temperature. From 4 ms onwards, the recovery starts, divertor and upstream temperatures increase, whilst upstream density decreases due to pedestal fuelling. The term upstream denotes the location of the open field lines in the vicinity of the midplane, in contrast do downstream, which denotes the field lines in the vicinity of the divertor plates. All in all, the dynamics of the pedestal particle inventory is dominated by transient intense gas deposition into the plasma facing components and slow continuous gas release in the inter-ELM phase.

In addition to [31] reference [33] also observed a second peak in the outer divertor D_α signal, but at *ASDEX Upgrade*. At the time of this investigation, most of the plasma facing components were covered by tungsten coated tiles with the exception of the LFS limiters and the divertor target plates, which were composed of carbon fibre composite (CFC). This second peak is not accompanied by a drop in the plasma-stored energy or the line integrated electron density at the plasma edge. As a result, there is no release of power into the SOL and thus this cannot be a further ELM. At the maximum of the second peak of the D_α signal, whilst the particle flux is increased, the deposited power does not alter. Additionally, the electron temperature is suppressed as long as the second peak evolves.

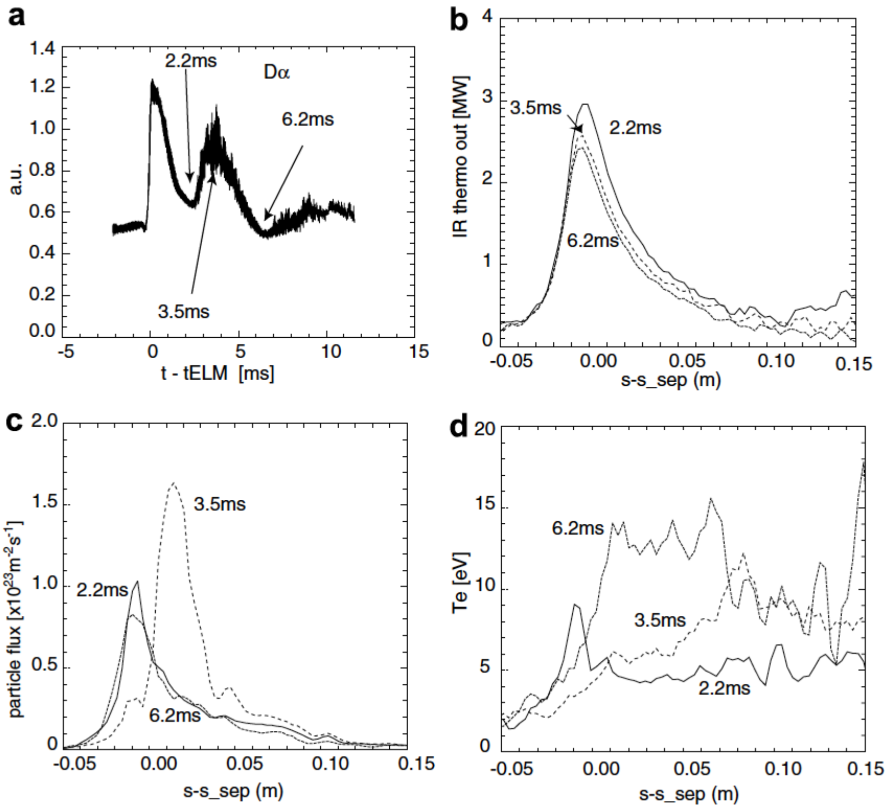

Figure 12: Coherent ELM averaged signals of (a) the D_α time trace and the outer target profiles for three distinct time slices during the second D_α peak: (b) power deposition profiles from IR, (c) particle flux and (d) T_e measured with Langmuir Probes. [33].

A transition from a non double peaked to a double peaked regime can be achieved through a electron density scan at constant heating power. There are two theories to explain the occurrence of the second peak. One involves the idea of instantaneous recycling, the method [31] uses to explain the second peak, wherein an ELM reaches the PFCs in less than 1 ms, and the lowest thermal speed of the resulting recycled flux molecules leads to a maximum time of flight of again $\ll 1$ ms. However, this is in discrepancy with the second peak onset of $\sim 4\,\mathrm{ms}$ or even $\sim 8\,\mathrm{ms}$ in [31]. The second theory describes the second peak as a sequence of transient upstream-downstream equilibria, linked by the *Two-point-model.* Equation 8 denotes the ratio of the target power flux Γ_t and the parallel power density $q_{||}$

$$\frac{\Gamma_t}{q_{||}} \propto \frac{n_u^{\frac{4}{7}}}{T_u^{\frac{10}{7}} T_t^{\frac{5}{7}}} \tag{8}$$

The target temperature T_t changes marginally, but due to the increase of that ratio, the upstream density n_u must increase faster than the upstream temperature T_u. However, at a certain point n_u saturates and T_u continues recovering. Reference [33] emphasizes that T_u is linked to the power crossing the SOL P_{SOL} and that P_{SOL} is the only energy source. A combination of refuelling through the separatrix and ionization sources due to recycled neutrals serve as pedestal particle sources.

In summary, these reviews show that the second peak phenomena can occur in different tokamak experiments. However, likely restricted to machines that are also tungsten covered. This peak can reach maximum values similar to the ELM, but the temporal extent varies. Despite its experimental occurrence being evident, the theory of its occurrence is still under investigation.
Reference [31] explains the second peak as a recycling effect, with its time delay linked to the penetration depth of deuterium in tungsten. Alternatively, [33] claims that the timescales of recycled particles do not coincide with the timescales of the occurrence of the second peak. Furthermore, [32] states that there is a constant inter-ELM outflux, and not a short transient one, which would be needed to explain the second peak D_α.

2.3 Magnetic oscillations in the inter-ELM phase

As mentioned in chapter 1.2 magnetic field lines can be subject to oscillations and fluctuations. These can have an impact on plasma behaviour, especially at the plasma edge. This chapter gives a rough summary of magnetic oscillation observations in the inter-ELM phase at different tokamak machines. Such oscillations of the radial magnetic field can usually be measured by magnetic pick up coils, see chapter 3.1.6. First of all, it is denoted that there is a differentiation between magnetic ELM precursor and non-precursor oscillations. According to [21], magnetic precursors can be observed prior to type-III ELMs and are classified by their increasing amplitude until a certain threshold, at which an ELM is triggered. In the following, precursor oscillations generally and non-precursor oscillations in other ELM regimes (e.g. type-II ELM related oscillations seen by [34, 22]) than type-I ELM regimes shall be excluded from the review, as only non-precursor oscillations in type-I ELM regimes are relevant in this thesis. The frequency range of magnetic oscillation observations of the following reviews reaches from 5 kHz to 500 kHz. This chapter orders the reviewed oscillations by decreasing frequency.

High frequency oscillations above 200 kHz are reported by [35] at *ASDEX Upgrade.* Figure 13 compares an ELM synchronized spectrogram of $\frac{\partial B_r}{\partial t}$ to the maximum gradient electron density $\max(\nabla n_e)$ and temperature $\max(\nabla T_e)$ evolution. Additionally, the inner divertor current is shown as an ELM indicator. Figure 13 shows a) a low and b) a high collisionality case. The high collisionality case shows that with the ELM crash, $\max(\nabla n_e)$ and $\max(\nabla T_e)$ collapse and the magnetic oscillations stop. With the end of the $\max(\nabla T_e)$ recovery (in this case around 6 ms), the onset of magnetic oscillations around 240 kHz can be clearly seen. However, these magnetic fluctuations are interrupted with the next ELM-onset.

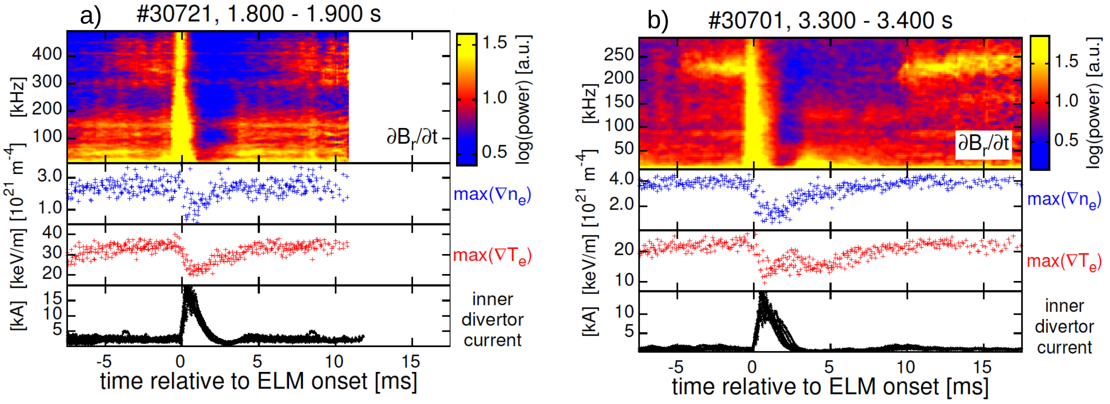

Figure 13: ELM-synchronised spectrogram of $\frac{\partial B_r}{\partial t}$ and ELM-synchronised time traces of $\max(\nabla n_e)$ (blue), $\max(\nabla T_e)$ (red) and inner divertor current (black) for the a) low collisionality case and b) high collisionality case. [35].

Similar observations can be made in the low collisionality case, although these oscillations show a larger frequency bandwidth and not such a high intensity for every ELM crash. Most important is the difference in the fluctuation frequency. As these oscillations vanish with an ELM, it is probable, that their location is in the pedestal region. Furthermore, these fluctuations have toroidal mode numbers of $n = 12$ and they are not ballooned, as these fluctuations also exist at the inboard midplane. In addition, reference [35] points out, that the detected magnetic oscillation frequency correlates with the edge $\vec{E}_r \times \vec{B}$ flow velocity.
Another report on high frequency oscillations is given by [36]. These frequencies of range 300 kHz to 500 kHz are only seen in low collisionality cases. Here a clamp of the edge T_e increase due to the onset of the high frequency oscillations, is observed.

Mid range (90 kHz to 150 kHz) and low (20 kHz to 50 kHz) frequency oscillations according to different plasma currents are observed by [37, 38] at the *DIII-D* tokamak and by [39] at the *Alcator C-Mod* tokamak.
Figure 14 shows a high, (b) and (d), and a low, (a) and (c), current case. In both cases an ELM synchronized spectrogram of $\frac{\partial B_r}{\partial t}$ reveals quasi-coherent fluctuations (QCF) in the low frequency range case (left) and the mid range case (right) above the plasma core mode and non ELM related broadband fluctuations (grey shaded area). These QCFs appear in the inter-ELM phase and disappear with an ELM crash. Reference [37] proposes a picture of these QCFs. After an ELM crash most

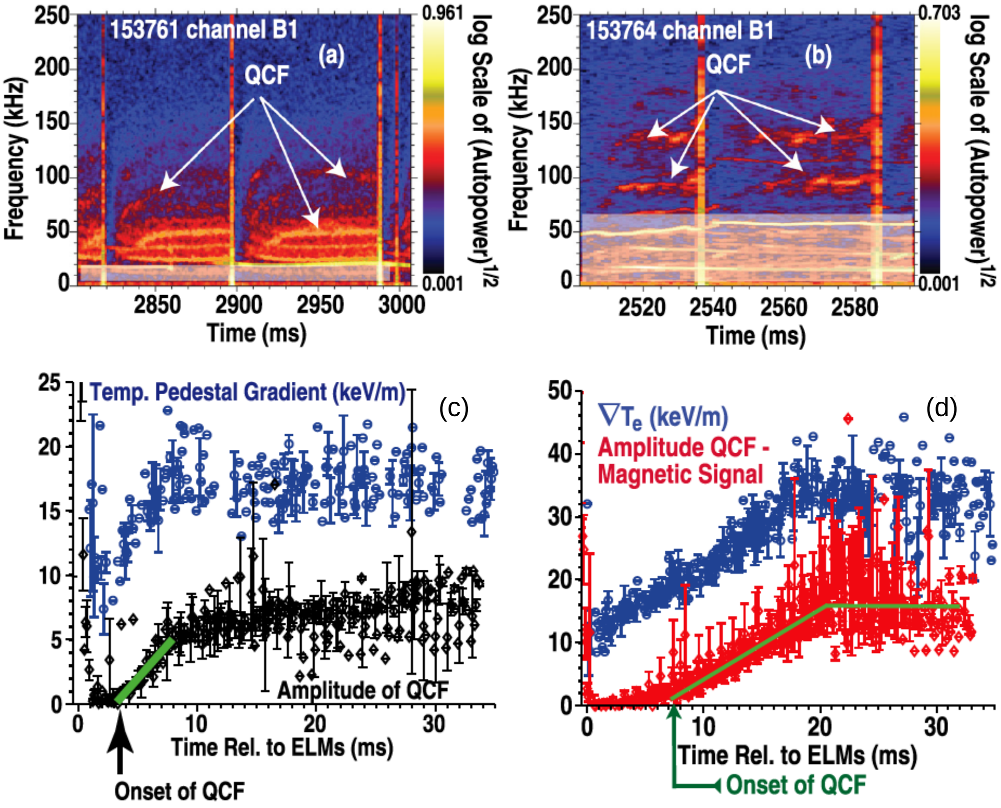

Figure 14: Inter-ELM magnetic fluctuations spectrograms showing the QCFs in low (a) and high (b) current cases. The shaded areas on the spectrograms represent the core modes and broadband fluctuations which are not ELM related events. The QCF amplitude's evolution relative to the ELM onset for the frequency bands (c) 23 kHz to 60 kHz and (d) 120 kHz to 170 kHz is shown together with the temperature gradient evolutions. [37].

of the electron heat can proceed from the core through to the pedestal. This heat helps building up the pedestal until a certain threshold gradient is reached. Exactly then QCF set in in the pedestal region, providing the necessary transport to limit the pedestal gradient growth. However, the pedestal height and width still build up. This close correlation between the oscillations and the ∇T_e evolution are shown in figure 14 for the c) low plasma current and d) high plasma current case.

At *JET*, so called washboard modes (WB) have been observed [40]. These magnetic broadband oscillations occur in the frequency range of 10 kHz to 90 kHz. Reference [40] states that these fluctuations are clearly linked to the pedestal evolution, as the WB modes follow the pedestal top T_e evolution. The sudden increase of WB modes leads to slower T_e buildup in the recovery phase and vice versa. Hence, this indicates a correlation of the WB modes and the enhanced energy transport across the SOL. Additionally, the amplitude of those WB modes is linked to the time between ELMs.

There are some similarities to the QCF seen at *DIII-D* and *Alcator C-Mod*: location in the pedestal region, rotation in direction of the electron diamagnetic drift, responsible for energy loss into the SOL. However, there are severe differences: discrepancy in the toroidal mode number, QCF is a single band opposed to WB broadband modes and QCFs have not been observed yet in other H-mode regimes.

All in all there is a wide range, 5 kHz to 500 kHz, of magnetic oscillations during the type-I inter-ELM phase. Most importantly, all of them correlate with the pedestal evolution and their location can be assumed in the pedestal region, as they vanish with the ELM-onset.

3 Used diagnostics and data analysis

For the purposes of this thesis, information about the plasma edge and the SOL from the midplane to the divertor at a reasonable ELM resolvable timescale was needed. Diagnostics, which are able to perform this task, will be described in the following chapters. Figure 15 shows an overview of the location and orientation of the diagnostics in a toroidal and poloidal cross section of *ASDEX Upgrade*.

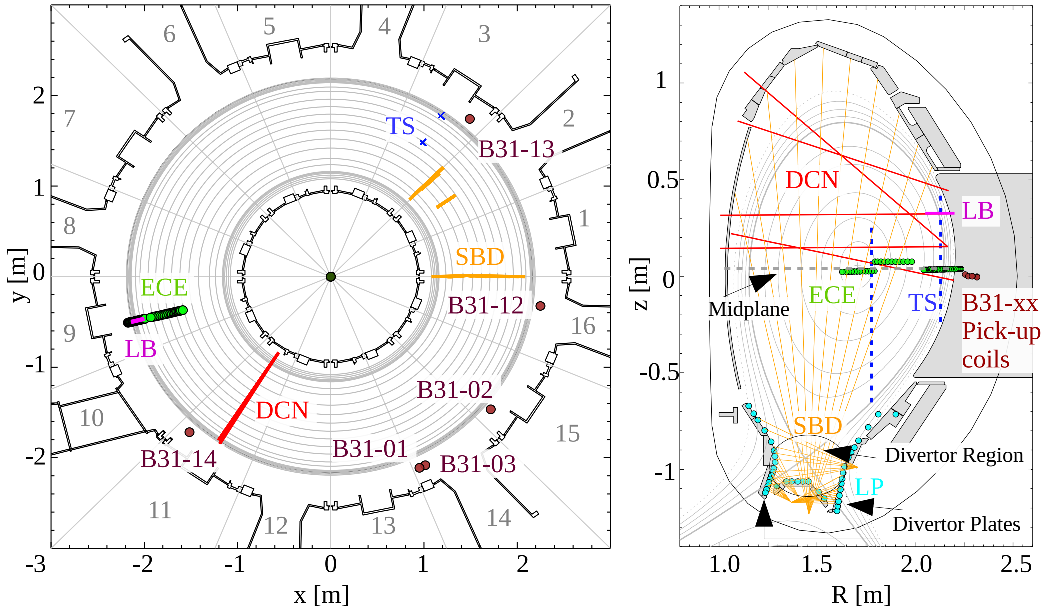
TS
B31-13
SBD
B31-12
ECE
LB
DCN
B31-02
B31-14
B31-01
B31-03
1
2
3
4
5
6
7
8
9
10
11
12
13
14
15
16
y [m]
x [m]
-3
-2
-1
0
1
2
DCN
LB
ECE
TS
B31-xx
Pick-up
coils
Midplane
SBD
Divertor Region
LP
Divertor Plates
z [m]
R [m]
1
0.5
0
-0.5
-1
1.0
1.5
2.0
2.5

Figure 15: Toroidal (left) and poloidal (right) cross sections of the *ASDEX Upgrade* Tokamak vessel. The diagnostics are shown in different colors: Lithium beam (magenta), electron cyclotron emission diagnostic (green), deuterium cyanide laser (red), pick up coils (brown), Stark broadening diagnostic (orange), Thomson scattering (blue) and the Langmuir probes (cyan). The LPs are not shown in the toroidal cross section.

3.1 Midplane diagnostics

The diagnostics at the midplane are denoted in figure 15. The diagnostics used here are the Lithium beam impact excitation spectroscopy, the electron cyclotron emission, the Thomson scattering, the deuterium cyanide laser interferometry, the pick up coils and the integrated data analysis. These will be described in the following.

3.1.1 Lithium beam impact excitation spectroscopy

The Lithium beam (LB) diagnostic is a tool designed to measure the electron density in the SOL and the pedestal [41, 42, 43, 44, 45, 46, 47, 48].

A sketch of the setup of the LB at *ASDEX Upgrade* can be seen in figure 16. Li^+ ions get extracted from an emitter electrode (at 50 kV and heated with $\sim$ 200 W)

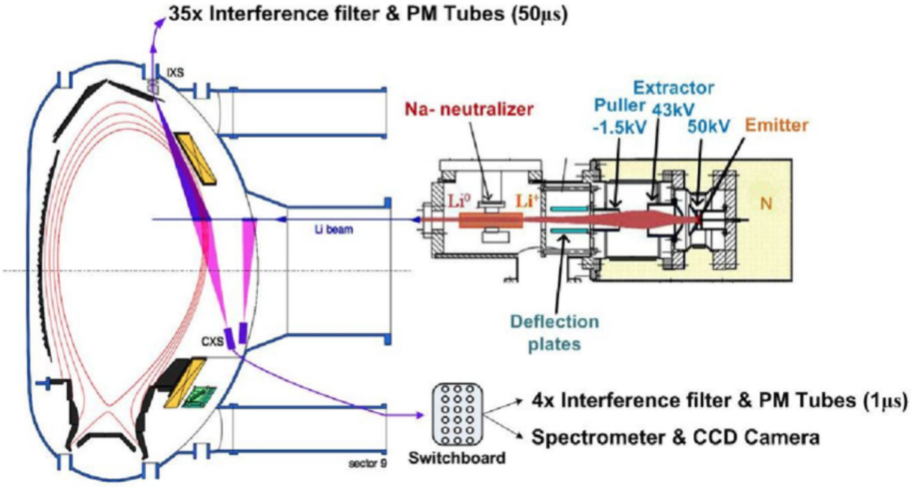
35x Interference filter & PM Tubes (50µs)
IXS
Na- neutralizer
Extractor
Puller
43kV
-1.5kV
50kV
Emitter
Li^0
Li^+
N
Li beam
Deflection plates
CXS
4x Interference filter & PM Tubes (1µs)
Spectrometer & CCD Camera
Switchboard
sector 9

Figure 16: Schematic sketch of the Lithium beam emission spectroscopy setup [49].

by an extractor at 43 kV. This extractor also focuses the beam before the Li^+ ions are accelerated by the puller electrode. To prevent secondary electrons flying back and causing damage to the emitter electrode, this puller electrode is set at a negative potential of -1.5 kV. After further adjustment of the beam through deflection plates, the Li^+ ions enter a sodium (Na) neutralizer cell. These Na atoms (alkali metal) transfer their valence electrons onto the Li^+ ions through charge exchange processes and therefore neutralize them. These Li atoms now enter the SOL and the confined plasma. Here they interact with the plasma particles through several reactions:

- Excitation by collisions with plasma particles
- De-excitation by collisions with plasma particles
- Ionization
- Charge exchange processes

These processes can be described by a set of coupled differential equations:

$$\frac{dN_i(z)}{dz} = [n_e(z)a_{ij}(T_e(z)) + b_{ij}]N_j(z) \tag{9}$$

$$N_i(z = 0) = \delta_{1i} \tag{10}$$

N_i indicates the number of Li atoms in the state i ($i = 1$ stands for the ground state Li(2s), $i = 2$ for the first excited state Li(2p) and so forth), z the beam axis. Thus equation 10 denotes, that the Li atoms are in ground state at the beam entrance $z = 0$. The coefficients a_{ij} ($i \neq j$) represent excitation and de-excitation from state i to state j and vice versa. Charge exchange, ionization and transitions to states $j > 9$ (considered the same as ionization) are denoted by a_{ii}. Since these are collisional interactions, they are dependant on the electron temperature $T_e(z)$

and on the electron density $n_e(z)$ along the beam line. The b_{ij} Einstein coefficients describe spontaneous emission.
The lithium beam impact excitation spectroscopy (Li-IXS) or lithium beam emission spectroscopy (Li-BES) uses the $Li(2p \rightarrow 2s)$ transition line (670.8 nm) intensity to deduce the corresponding occupation number of the $Li(2p)$ state N_2.

$$N_2(z) = \alpha \cdot I_{Li(2p \rightarrow 2s)} \tag{11}$$

A probabilistic data analysis approach, using Bayesian probability theory (BPT) can be used to obtain the electron density profile [50]. Starting from the wall along the z-axis the $Li(2p \rightarrow 2s)$ intensity increases with electron density n_e. However, as the plasma reaches a certain density the increasing ionization rate will lead to a decrease in the probability of populating the $Li(2p)$ state and therefore a decrease of the $Li(2p \rightarrow 2s)$ intensity.
This emission line is mainly observed around the separatrix by two optical systems, one from the top and one from the side [51]. This optical system has recently been improved along with other upgrades like the new beam chopping system and the faster data acquisition system [52].

3.1.2 Electron cyclotron emission measurement

Electron cyclotron emission (ECE) can be used to deduce the electron temperature T_e. Accelerated electrons emit electromagnetic waves. As circular motion is an accelerated motion, gyrating electrons emit photons at a certain frequency ω:

$$\omega = n \cdot \omega_{ce} = n \cdot \frac{eB}{m_e} \tag{12}$$

The integer n expresses, that the emitted frequency is not only possible at its cyclotron radiation frequency, but also at its higher harmonics. The electron mass is denoted by m_e, the elementary charge by e and the magnetic field strength by B. However, this magnetic field strength is not constant in the plasma vessel, see chapter 1.1.2, therefore different frequencies at different points lead to a spatial resolution, already at a single line of sight.
If the electron density n_e and temperature T_e is high enough, then the plasma optically thickens (which is the case in the plasma). This means that all radiation is absorbed by the cyclotron resonance, and thus the plasma behaves and emits like a black-body radiator. Hence, the electron temperature T_e can be deduced from the emitted radiation intensity, according to the Rayleigh-Jeans approximation, which is applicable for present day fusion plasmas ($h\nu(< 1\,\mathrm{meV}) \ll kT(> 10\,\mathrm{eV})$), of Planck's law for black-body radiation:

$$I_{BB} = \frac{\omega^2}{4\pi^2 c^3} \cdot kT_e \tag{13}$$

One can directly deduce with equation 12 and 13 the electron temperature T_e by measuring the radiation intensity and its corresponding microwave frequency with a heterodyne radiometer [53].
However, at high T_e gradients and low n_e (this is the case at the plasma edge slightly

outside the separatrix) ECE measurements produce artefacts and fail to assess the correct T_e. This phenomena (shine through effect) is caused by strongly down-shifted radiation of Maxwellian tail electrons located at the plasma edge [20]. To resolve this problem Bayesian probability theory (BPT) can be applied for joint analysis of the electron density and temperature with data of different interdependent and complementary diagnostics [54], see chapter 3.1.5.

3.1.3 Thomson scattering diagnostic

Electron temperature T_e and density n_e of a plasma can be obtained using the Thomson scattering (TS) effect. A photon hitting a charged particle can be described as an elastic collision, wherein a fraction of the energy of the photon transforms into kinetic energy of the particle. This results in a reduction of frequency and increase in wavelength of the electromagnetic wave. This phenomenon is called the Compton scattering effect.

The Thomson scattering effect is the same as the Compton effect, but at a much lower photon energy compared to the mass energy of the charged particle ($\nu \ll mc^2/h$). This is equivalent to the wavelength of the electromagnetic wave being much greater than the Compton wavelength of the particle.

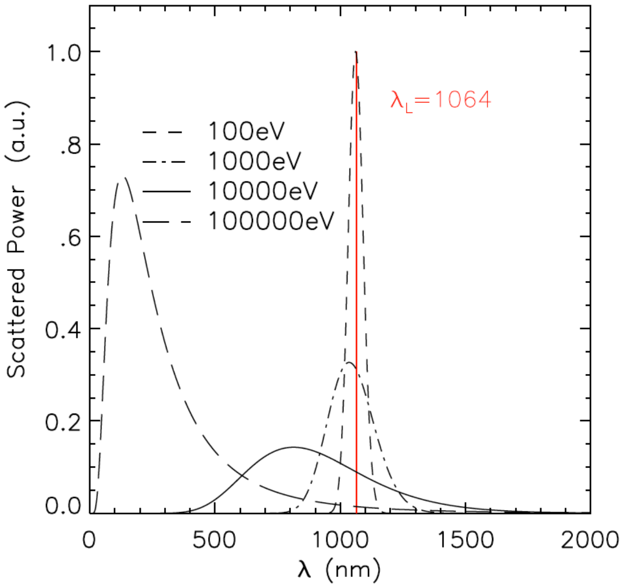

Figure 17: Spectral distribution of scattered power from a Nd:YAG laser [55]

In plasma it is predominantly electrons oscillating in the electromagnetic field, owing to their $\sim 10^3$ fold lower mass than protons. This oscillation is an accelerated motion, thus an electron acts as a dipole and emits light relative to this oscillation frequency. However, this emitted frequency is Doppler shifted twice due to the electron motion relative to the incident wave and the electron motion relative to the outgoing wave.

$$\Delta\omega = \vec{v} \cdot \vec{k}_{in} - \vec{v} \cdot \vec{k}_{out} = \vec{v} \cdot \vec{k} \tag{14}$$

The Doppler shift is denoted by $\Delta\omega$, the electron velocity by $\vec{v}$ and the wave number $\vec{k}$ is the subtraction of the incident and scattered wave number $\vec{k} = \vec{k}_{in} - \vec{k}_{out}$. As the difference is very small ($k_{in} \approx k_{out}$), the wave number can be approximated by $k \approx 2k_{in} \cdot sin\frac{\Theta}{2}$.

$$\alpha = \frac{1}{k\lambda_D} \approx \frac{1}{2k_{in}\lambda_D sin(\frac{\Theta}{2})} = \frac{1}{4\pi sin(\frac{\Theta}{2})}\frac{\lambda_{in}}{\lambda_D} \tag{15}$$

The scattering parameter α expresses the ratio of the incident wavelength λ_{in} and the Debye length $\lambda_D \propto (\frac{T}{n})^{\frac{1}{2}}$ [56]. This Debye length is the length at which the potential of an ion is screened by electrons to the $\frac{1}{e}$-fold of its original value. This inherits that a greater Debye length is due to fewer electrons which can screen the ion. Consequently, if $\alpha \ll 1$ (applicable for present day Tokamaks [57]), there are mostly individual electrons that scatter the incident beam. Hence, the scattering parameter α and the Doppler shifted scattered spectrum reflect the velocity distribution of the electrons. If the electron velocity distribution is Maxwellian, then the scattered spectrum is Gaussian and its half width is proportional to $T^{\frac{1}{2}}$ [57]. Furthermore, the electron density n_e can be deduced by measuring the intensity of the scattered radiation. Figure 17 depicts the theoretical scattered spectra at different electron temperatures. With higher temperature the Gaussian moves further to lower wavelengths and its shape becomes more asymmetrical.

Clusters of 4 and 6 Nd:YAG (neodymium-doped yttrium aluminium garnet) lasers with pulse energies of 1J, pulse durations of 15 ns each and with a wavelength of $\lambda_{in} = 1064\,\text{nm}$ are used for measurements at the core and at the plasma edge at *ASDEX Upgrade* [58]. The sampling rate reaches values of 8.3 ms at the edge and 12.5 ms in the plasma core.

3.1.4 Deuterium cyanide laser interferometry

A deuterium cyanide laser (DCN) can be used to measure the electron density n_e at the edge and in the core of the plasma. This diagnostic makes use of the dependency of the refraction index N on the electron density n_e. However, this relation only holds for a laser frequency ω_0 above the electron plasma frequency ω_{pe}.

$$N \approx 1 - \frac{\omega_{pe}^2}{2\omega_0^2} = 1 - \frac{e^2}{2\epsilon_0 m_e \omega_0^2} \cdot n_e \tag{16}$$

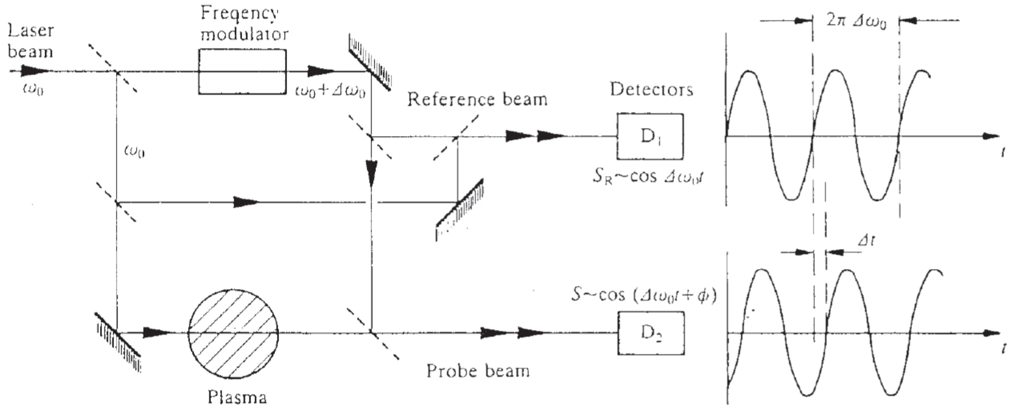

Figure 18: Deuterium cyanide laser interferometry sketch [59]

Figure 18 shows a sketch of a DCN setup using a Mach-Zehnder interferometer. This laser beam is split into three parts. The first passes through the plasma and changes its phase according to its underlying refraction index, the second is the reference beam which is unaltered, and finally the third beam is modulated and added to the other two, so that the resulting frequency is not in the range of the original laser beam, but in between 10 kHz and 100 kHz. One can obtain the phase shift between the reference beam and the plasma beam by measuring their signals at two different detectors. This phase difference is dependent on the line integrated electron density:

$$\Delta\Phi \approx \frac{e^2}{2c\epsilon_0 m_e \omega_0} \int_L n_e dl \tag{17}$$

At *ASDEX Upgrade* the DCN laser (wavelength about 195 µm) uses five channels and therefore can obtain line integrated electron density measurements at five different line of sights, each of them with a time resolution of 300 µs.

3.1.5 Integrated data analysis

Integrated data analysis (IDA) is a tool to combine several complementary diagnostics in a probabilistic manner.
Rather than simply combining the results from each diagnostic, IDA provides a combination of the raw data of each diagnostic and their corresponding uncertainties simultaneously in the framework of Bayesian probability theory (BPT) [60].

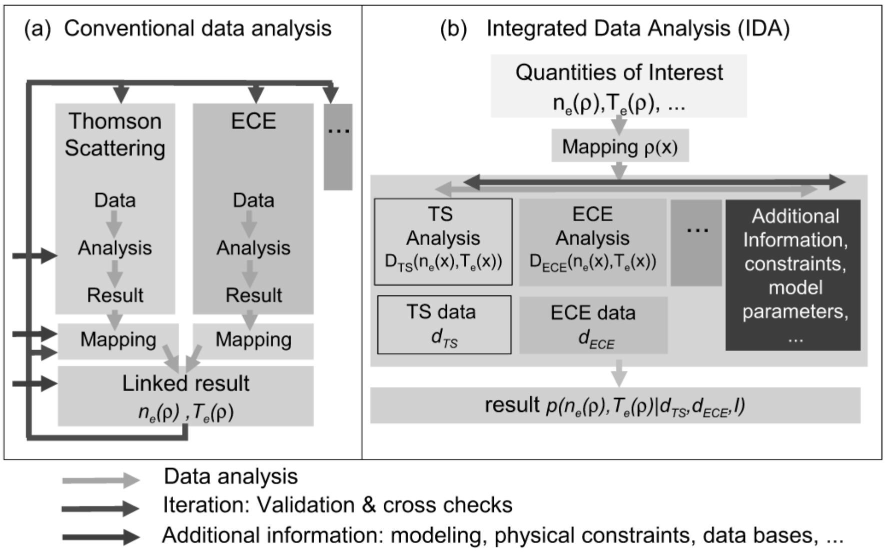
(a) Conventional data analysis
Thomson Scattering
ECE
...
Data
Analysis
Result
Data
Analysis
Result
Mapping
Mapping
Linked result
$n_e(\rho)$, $T_e(\rho)$
(b) Integrated Data Analysis (IDA)
Quantities of Interest
$n_e(\rho)$, $T_e(\rho)$, ...
Mapping ρ(x)
TS Analysis
$D_{TS}(n_e(x),T_e(x))$
ECE Analysis
$D_{ECE}(n_e(x),T_e(x))$
...
Additional Information, constraints, model parameters, ...
TS data
d_{TS}
ECE data
d_{ECE}
result $p(n_e(\rho),T_e(\rho)|d_{TS},d_{ECE},I)$
Data analysis
Iteration: Validation & cross checks
Additional information: modeling, physical constraints, data bases, ...

Figure 19: Schematic comparison of the (a) conventional data analysis with the (b) IDA approach [60].

This joint optimization process leads to a set of parameter values most likely to fit the measured data. Within the Bayesian approach a priori information can be fed to the calculation, constraining possible solutions, e.g. positive density and temperature profiles, smoothness and monotony. The probability of such preexisting information is quantified by the prior probability density function (PDF) $p(x, y)$. The likelihood PDF $p = (d|x, y)$ contains the experimental data, expressing the probability of measuring d with parameter values x and y. Bayes' theorem

$$p(x, y|d) = \frac{p(d|x, y)p(x, y)}{p(d)} \tag{18}$$

of the posterior PDF $p(x, y|d)$ denotes the probability to obtain the values x and y if d is measured. Maximizing these posterior PDFs results in parameter values which best fit the measured data set.

The electron density n_e and temperature T_e profiles are of interest at *ASDEX Upgrade*, thus IDA is applied using data from the LB and DCN diagnostics to obtain electron density n_e data and ECE for electron temperature T_e data.

Due to its lower temporal resolution the TS diagnostic is not used for feeding data into IDA, but it is used to align the n_e with the T_e profile, as the TS diagnostic measures n_e and T_e simultaneously at the same position leading to a relative alignment of ECE and LB with an accuracy of 5 mm [61].

Each of these diagnostics uses the forward modelling approach, generating values for the measured data. In order to obtain the likelihood probability density function L (Gaussian or Cauchy distribution [62]), the deviation between the modelled data D and the raw data d weighted with the measurement uncertainties needs to be calculated.

Maximizing the posterior PDF

$$P_{posterior} \propto L_{LIB} \cdot L_{DCN} \cdot L_{ECE} \cdot P_{prior} \tag{19}$$

leads to the most probable electron density and temperature profiles compatible with all the measurements and the above-mentioned a priori constraints. IDA provides consistent n_e results from $\rho_{pol} = 0$ til $\rho_{pol} = 1.2$, but leads to difficulties for the T_e profile in the optically thin region outside the SOL, due to the shine through effect. ρ_{pol} denotes the normalized poloidal radius.

3.1.6 Pick up coil measurements

Pick up coils are used for measurements of the alteration of the magnetic field lines in the plasma vessel. Thus, they are able to measure e.g. magnetic fluctuations due to instabilities. A pick up coil is based on the principle of the Maxwell-Faraday equation:

$$\vec{\nabla} \times \vec{E} = \frac{\partial \vec{B}}{\partial t} \tag{20}$$

A temporal change in the magnetic field leads to an induced current in a coil. Hereby, the amplitude of the voltage is a direct indicator for the rapidness of change of the magnetic field. In *ASDEX Upgrade* a number of these pick up coils are installed, measuring the poloidal and radial magnetic field changes, $\dot{B}_p$ and $\dot{B}_r$.

3.2 Divertor region diagnostic

The divertor region is denoted in figure 15, as well as the Stark broadening diagnostic, which will be described in the following.

3.2.1 Stark broadening diagnostic

The Stark broadening diagnostic (SBD) uses the Stark effect to obtain the electron density n_e in front of the divertor, the so-called divertor region or divertor volume. Thereby, this effect is proportional to the density of the surrounding particles. As the Langmuir probes can only provide information at the divertor, this diagnostic, which was recently installed, is especially useful to obtain information about the electron density in the detached regime, in which most of the plasma is in the divertor volume and does not reach the target [63]. This Stark broadening effect is a quantum mechanical effect that leads to the shifting and broadening of the upper principle quantum number n in an electric field. In plasma, this broadening is a combination of the pressure broadening due to Coulomb collisions (collision damping theory) and the Stark splitting due to the electric field produced by surrounding charged particles (statistical theory). If the perturbation time is short in comparison to the time of interest, then the collision damping theory is applicable, determining the center of the emitted spectral line. The statistical theory is valid in the opposite case and is responsible for the shape of the line wings of this spectral line, see also figure 20.

At *ASDEX Upgrade* this diagnostic uses the deuterium $\mathrm{D}_\epsilon(7 \rightarrow 2)$ or $\mathrm{D}_\delta(6 \rightarrow 2)$ Balmer spectral lines, compromising between the more pronounced Stark broadening effect and the signal-to-noise ratio at higher upper principle numbers.

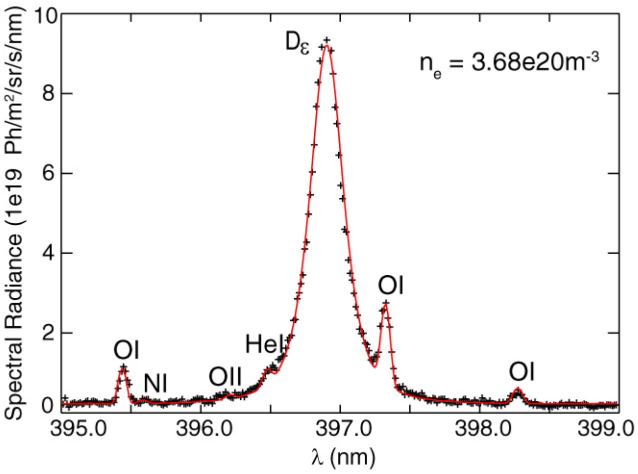

Figure 20: Spectral radiance versus wavelength. Example fit to the D_ϵ line yielding n_e [63].

A semi-quantum mechanical approach to combine the pressure broadening by electrons and the Stark splitting caused by ions is described in the so called *unified theory* [64]. However, pressure broadening by ions cannot be included in this theory. Therefore, another approach that includes the pressure broadening by ions is the *model microfield method* (MMM) [65]. The theoretical Stark profiles, following the above mentioned theories, can be fitted to the measured Balmer lines, determining the spectral line shape parameters and therefore the electron density.
The current Stark broadening diagnostic at *ASDEX Upgrade* can provide electron density measurements for 11 lines of sight (LOS) at 3500 time frames. Along one LOS, the density measurement is localized to the region with highest emissivity, therefore it is not an averaged density of the LOS pathway. However, at densities lower than $4 \times 10^{19} \frac{1}{\mathrm{m}^3}$ the Doppler effect increases such that the Doppler profile becomes comparable to the Stark profile and the above mentioned theories are not applicable anymore. Additionally, the divertor should be in the medium to high recycling regime in order to provide a reasonable signal-to-noise ratio.

3.3 Divertor target diagnostic

The divertor consists of the outer and the inner target plates, as denoted in figure 15. There are several Langmuir probes flush-mounted in the divertor plates. The concept of a Langmuir probe will be described in the following.

3.3.1 Langmuir probes

Langmuir probes (LP) are robust devices to obtain plasma properties, like electron density and temperature. There are many LPs installed in the vessel, but those used here are placed on the divertor target plates.
By applying a voltage sweep to the probe head, the resulting current from the plasma can be measured via a shunt resistance. This leads to a current-voltage characteristic, see figure 21, from which the electron density and temperature, ion

density, floating and plasma potential and the electron energy distribution can be derived.

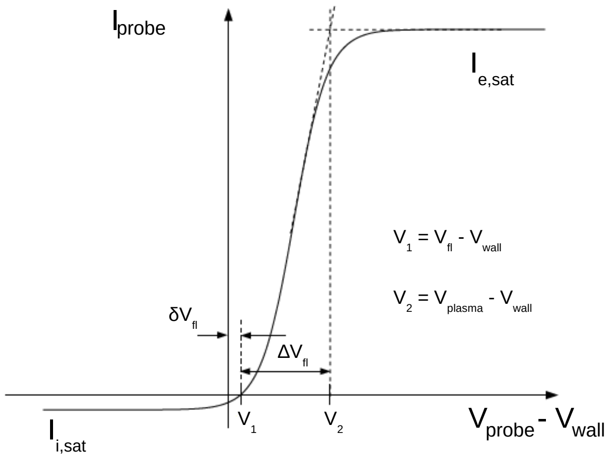

Figure 21: Theoretical current-voltage characteristic of a Langmuir probe. All potentials denoted here are relative to the vessel potential [66].

The current at the probe consists of the ion and the electron current:

$$I_{probe} = -A_{probe}\ j_{i,sat} + A_{probe}\ j_{e,th}\ e^{\frac{(V_{probe}-V_{plasma})e}{k_B\ T_e}} \tag{21}$$

$j_{e,th}$ denotes the thermal electron current density, $j_{i,sat}$ the ion saturation current density, A_{probe} the probe head surface, k_B Boltzmann's constant, e elementary charge, V_{probe} the applied potential at the probe head and V_{plasma} the potential of the plasma.

At negative probe potential, only positively charged ions will reach the probe head. With increasing voltage, more and more electrons, assumed to be distributed in a Maxwellian manner, will be able to reach the probe head. The voltage referring to the point where the electron and ion current cancel each other out $I_{probe} = 0$, is called the floating potential V_{fl} ($V_{fl} = V_{probe}$ at $I_{probe} = 0$):

$$\Delta V_{fl} = V_{fl} - V_{plasma} = \frac{k_B\ T_e}{e}\ ln\Big(\frac{I_{i,sat}}{I_{e,th}}\Big) \tag{22}$$

The electron temperature T_e can be derived from inserting equation 22 into equation 21 by eliminating the unknown V_{plasma}:

$$\frac{k_B\ T_e}{e}\ ln\Big(\frac{I_{probe}+I_{i,sat}}{I_{e,th}}\Big) - V_{probe} = V_{plasma} = V_{fl} - \frac{k_B\ T_e}{e}\ ln\Big(\frac{I_{i,sat}}{I_{e,th}}\Big)$$

$$T_e = \frac{e}{k_B}(V_{probe} - V_{fl})\ \Big[ln\Big(1+\frac{I_{probe}}{I_{i,sat}}\Big)\Big]^{-1} \tag{23}$$

Thus, T_e can be determined by applying V_{probe} and measuring its resulting current I_{probe} at a certain value of the floating potential V_{fl} and ion saturation current $I_{i,sat}$.

V_{probe} is usually a sawtooth-shaped voltage, with its periodic frequency resulting in the temporal resolution of the T_e measurement.
The electron density n_e can be derived, using this result for T_e, under reasonable assumptions for the sonic speed c_s, at which ions, that transit from the quasi neutral plasma into the electrostatic sheath travel [67], and quasi neutrality:

$$c_s = \left(\frac{k_B(Z\, T_e + \gamma\, T_i)}{m_i}\right)^{\frac{1}{2}} \tag{24}$$

The electron density results in

$$n_e = Z\, n_i = \frac{I_{i,sat}}{A_{probe}\; e\; c_s} \tag{25}$$

This basic technological approach ensures reliable measurements of the plasma parameters in front of the probe by determining the voltage-current characteristic. A long list of Langmuir Probes are integrated in the *ASDEX Upgrade* setup, delivering robust measurements for j_{sat}, n_e and T_e in a time resolution that is able to resolve ELM events in detail.

4 Experimental investigation of the inter-ELM phase

In order to understand the plasma edge behaviour it is necessary to understand the relation between the midplane and the divertor plates. This relation is affected by ELMs and the resulting gradient recovery. Chapter 4.1 describes the influence of the deuterium fuelling on the inter-ELM phase at the midplane in chapter 4.1.1, the divertor plates in 4.1.2 and on the midplane fluctuations, chapter 4.1.3. Furthermore, chapter 4.2 shows that the outer midplane, the outer divertor and the midplane fluctuations at the low magnetic field side are linked. A characterization of distinct midplane fluctuations and outer divertor phases will be presented in compliance with existing midplane phases descriptions [25, 26].

4.1 Influence of the deuterium fuelling rate

This chapter presents a selection of five different deuterium fuelling rate phases. As this was not performed in a single shot, an accurate selection of phases of different shots needed to be chosen.

shot	Δt [s]	$D_{tot}[10^{21}\frac{1}{s}]$	$P_{tot}[10^6W]$	$f_{ELM}[Hz]$	$W_{mhd}[10^5J]$
31547	5.6-6.0	0.02	4.36	37.6	4.56
31513	4.3-4.9	5.73	4.17	36.5	4.47
31513	3.5-3.8	7.72	4.19	57.3	4.03
31513	2.2-2.6	8.67	4.27	61.6	3.96
30701	2.975-3.4	11.5	5.32	70.6	3.83

Table 2: Selection of shot ranges with increasing deuterium fuelling D_{tot} and ELM frequency f_{ELM} and decreasing MHD plasma stored energy W_{mhd}. The total heating power P_{tot} is almost held constant, except for shot 30701. The plasma current I_p is held at $\sim 1.05\,\text{MA}$, the toroidal magnetic field at $\sim -2.5\,\text{T}$. All these values are averaged over the denoted time interval.

All the following investigations have been performed by using the shot ranges, given in table 2. They seem to be reasonably comparable, except for 30701, which is the odd one out regarding the inter-ELM evolution at the midplane and divertor shown later, probably due to its higher total heating power P_{tot}.

4.1.1 Outer midplane

This chapter investigates the deuterium fuelling influence on the midplane electron density and temperature evolutions. Figure 22 shows time traces of the electron density at $\rho_{pol} = 0.98$ and 1.01 as well as the electron temperature evolution at $\rho_{pol} = 0.94$, synchronized to the ELM onset. This data has been obtained through the IDA framework explained in chapter 3.1.5, using information of the lithium beam emission spectroscopy for the plasma edge density and the deuterium cyanide

laser interferometry for the plasma core density as well as the electron cyclotron emission for the plasma edge temperature.
There is a big difference between the densities at $\rho_{pol} = 1.01$ and 0.98 in the pre-ELM phase, denoting the steep edge gradients. With the ELM the pre-ELM density values according to each fuelling regime at $\rho_{pol} = 0.98$ crash at 0 ms and then recover quickly initially but then at a decelerated rate. However, the density overshoots slightly the pre-ELM values before reaching pre-ELM values at times beyond 11 ms. It can be seen that the higher the deuterium fuelling the higher the densities throughout the whole evolution, except for the blue line of shot #30701. In this discharge the strike lines are placed lower, close to the pump duct, enabling a better pumping in the divertor.

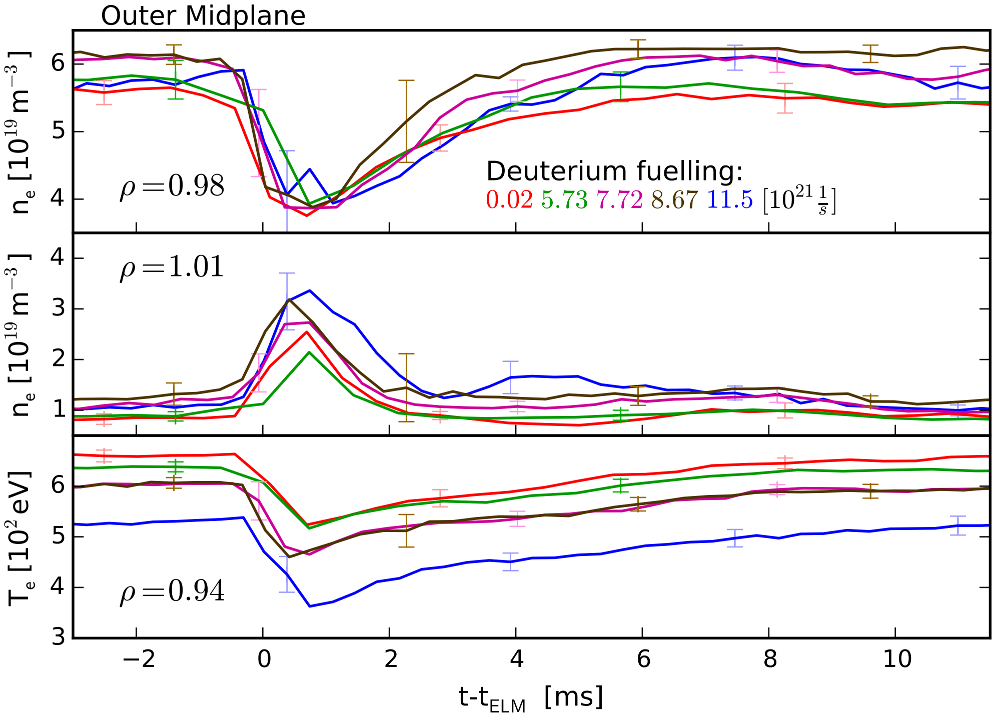

Figure 22: ELM synchronized density ($\rho_{pol} = 0.98$ and $\rho_{pol} = 1.01$) and temperature ($\rho_{pol} = 0.94$) evolutions at the outer midplane for different deuterium fuelling regimes (red: $0.02 \times 10^{21} \frac{1}{s}$, green: $5.73 \times 10^{21} \frac{1}{s}$, magenta: $7.72 \times 10^{21} \frac{1}{s}$, brown: $8.67 \times 10^{21} \frac{1}{s}$, blue: $11.5 \times 10^{21} \frac{1}{s}$)

The same holds for the density evolution at $\rho_{pol} = 1.01$. However there is an increase in density outside the separatrix ($\rho_{pol} = 1.00$) due to the ELM crash, with its density disappearing after the ELM. Additionally, there is a small density hump with its maximum around 8 ms in all fuelling regimes except for the blue $D_{tot} = 11.5 \frac{1}{s}$ case, where a pronounced density hump can be observed around 4.2 ms. The temperature evolution at $\rho_{pol} = 0.94$ shows a temperature crash as well, however the following recovery phase lasts longer than the density recovery phase. Additionally, it can be seen that less deuterium fuelling leads to a higher temperature throughout the whole evolution.

4.1.2 Inner and outer divertor

This chapter reveals the influence of the deuterium fuelling on the divertor electron density and temperature inter-ELM phase by synchronizing ELMs to their onsets. The electron density and temperature have been measured with the Langmuir probes, that are flush-mounted in the divertor plates, see chapter 3.3.1. Figure 23 shows such a typical ELM synchronized measurement for the outer divertor (right) by using the ua5 Langmuir probe (closest probe located above the strikeline) and the inner divertor (left) by using the Langmuir probes ui7 and ui8 (closest two probes located above the strikeline) oh shot range #31513, 3.5-3.8 s. The purple line shows the moving average of the scattered data. Around 0 ms one can clearly see the ELM occurrence in the inner and outer divertor electron density and temperature. Additionally, the phase after the ELM shows an interesting evolution before it reaches pre-ELM values again around 11 ms. This post-ELM phase will be discussed in detail later.

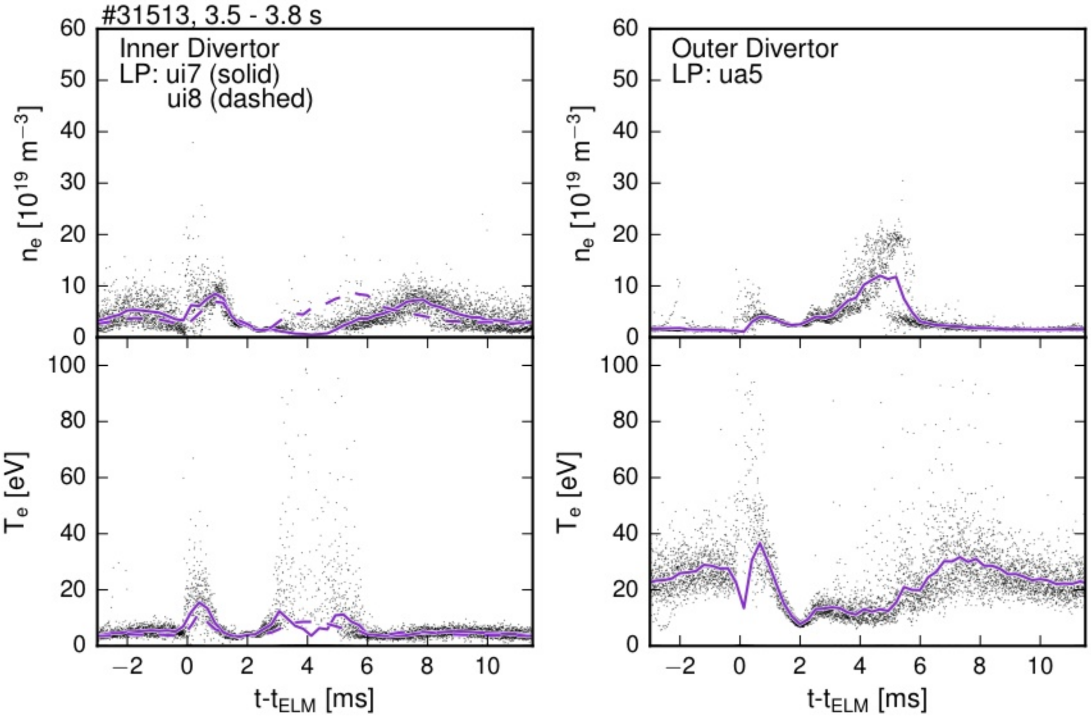

Figure 23: ELM synchronized electron density n_e and temperature T_e evolution at the inner (left) and the outer (right) divertor plates for shot 31513 in the time range of 3.5 s to 3.8 s. The magenta continuous line denotes the moving average of the scattered data. Note that not all data points are shown in the inner divertor density plot, as a few data points scattered up to values of $130 \times 10^{19}\,\frac{1}{\mathrm{m}^3}$.

As there are many Langmuir probes in the divertor plates it is necessary to find out the inter-ELM evolution relevant regions. Therefore a characteristic single ELM density evolution is shown in figure 24 at the inner (bottom) and outer (top) divertor plate together with the according equilibria in an enlarged poloidal cross section of the plasma vessel . The position of four LP is shown to the right and the according electron density measurements to the left. The equilibria, shown to the right, contain

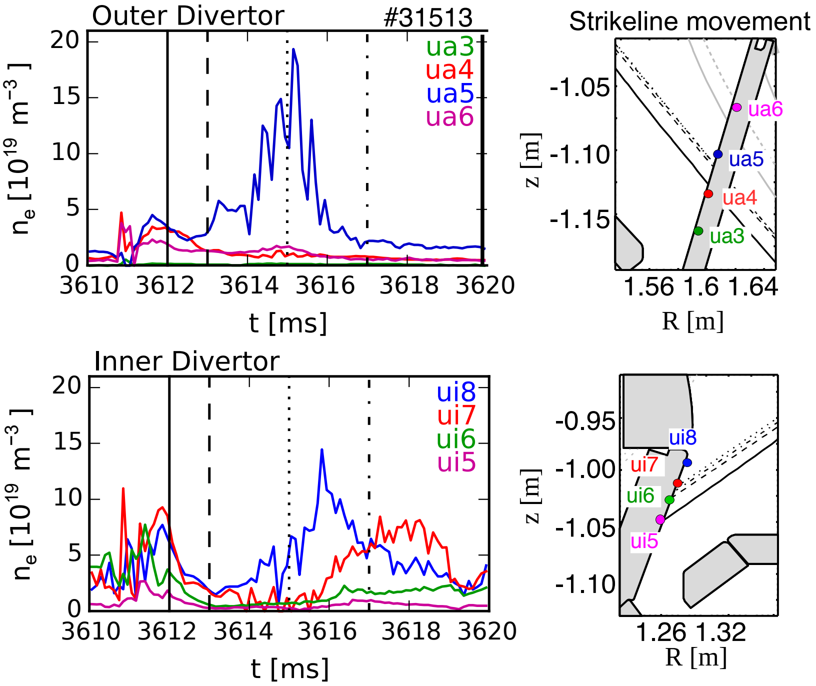

Figure 24: On the left: Single ELM density evolution at 4 different Langmuir probes at each divertor plate for shot 31513. Langmuir probes at the outer divertor are denoted by ua3: green, ua4: red, ua5: blue, ua6: magenta and at the inner divertor ui5: magenta, ui6: green, ui7: red, ui8: blue. On the right: Enlarged poloidal cross section of the outer (top) and inner (bottom) divertor plates with the color coded Langmuir probes. The black continuous line denotes the separatrix (strikeline) at the time point 3.612 s, the dashed line at 3.613 s, the dotted line at 3.615 s and the dashed-dotted line at 3.617 s.

the separatrices or strike lines according to the time points 3.612 s (solid black), 3.613 s (dashed black), 3.615 s (dotted black) and 3.617 s (dashed-dotted black).

At 3.612 s (solid black line), which is shortly after the ELM onset it can be seen at the outer divertor that the LP ua4 (red), ua5 (blue) and ua6 (magenta) detect the ELM signal. LP ua3 (green) does not detect a signal as this LP is located well below the strike line at this time point. One millisecond further (dashed black line), it can be seen that the strike line moved further up, almost back to its pre-ELM position. At the same time the signal at the LP ua5, which is the one slightly above the strike line, increases in contrast to the other LP ua3, ua4 and ua5. At time point 3.615 s (dotted black line) the post-ELM density maximum value is reached at LP ua5, far above the other LPs. This behaviour of the second density peak in the post-ELM phase being located around the LP which is the closest one above the strike line is characteristic for the outer divertor.

The inner divertor shows a slightly different behaviour. At 3.615 s (dotted black line) the strike line moves further up as well, but a bit further than its pre-ELM position, which is slightly above LP ui7 so that the second density peak is recorded initially at LP ui8. Two milliseconds later (dashed-dotted line) the strike line moves back to its pre-ELM position, which is slightly lower than the LP ui7 location. Accordingly, the inner density evolution shows a transition of measured data from LP ui8 to ui7. This underpins the assumption that most of the post-ELM electron density and temperature evolves in the vicinity above the strike line.

Due to this observation, all the following data will be shown with measurements of the first LP above the strike line at the outer divertor and the first and second LP above the strike line at the inner divertor, which differ from shot to shot.

A variety of different fuelling regimes according to table 2 are compared at the outer divertor electron density and temperature moving average evolution in figure 25. The ELM can be clearly seen in the density peak around 0 ms for all fuelling regimes. After the end of the ELM at ∼1.4 ms to 1.7 ms a phase with decreased electron density sets in til around 2.1 ms. From 2.1 ms on the build up of a second density peak starts. The density peak maximum reaches higher with higher deuterium fuelling rate levels. Around 7 ms to 8 ms the density of all shot phases reaches again pre-ELM values. However, the blue line is the odd one out, probably due to its higher total heating power P_{tot}. It shows a longer ELM, around 2 ms to 2.5 ms, a more smeared out second density peak and reaches pre-ELM values around 10 ms.

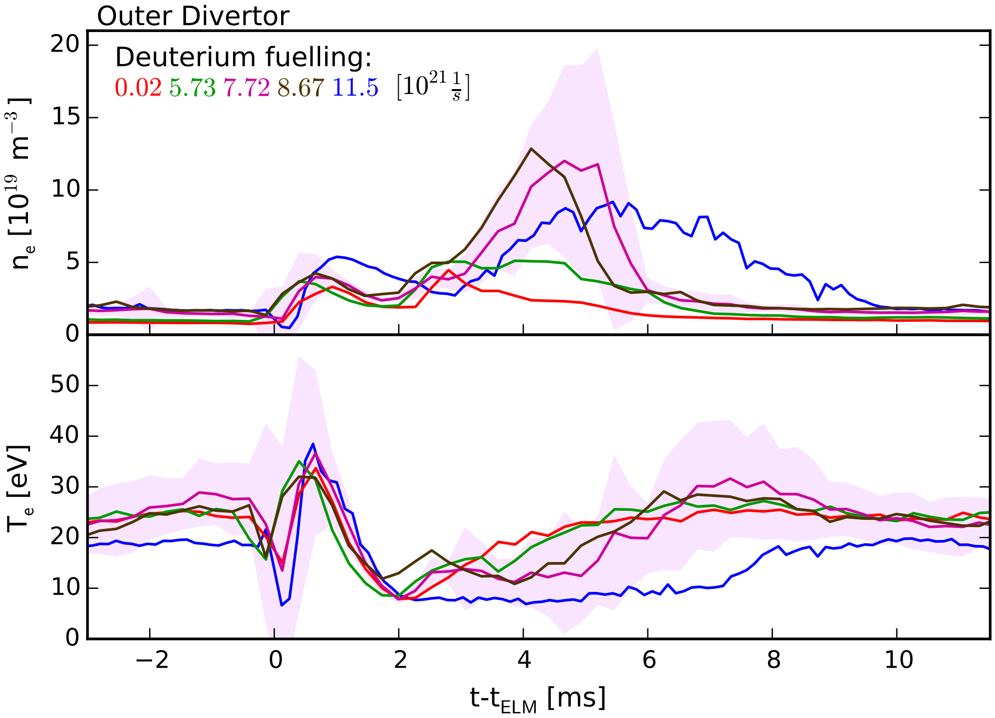

Figure 25: ELM synchronized electron density n_e and temperature T_e evolution at the outer divertor plates for five different deuterium fuelling regimes (red: $0.02 \times 10^{21}\,\frac{1}{s}$, green: $5.73 \times 10^{21}\,\frac{1}{s}$, magenta: $7.72 \times 10^{21}\,\frac{1}{s}$, brown: $8.67 \times 10^{21}\,\frac{1}{s}$, blue: $11.5 \times 10^{21}\,\frac{1}{s}$). The light magenta shaded area denotes the standard deviation to the magenta line.

The outer electron temperature shows a related evolution. After the ELM, around

2 ms, a quick increase can be observed til about 2.5 ms to 3 ms with a following stagnation until the density maximum is reached. This is different for each shot phase. The higher the density maximum peak the later but quicker the final temperature recovery. Again the blue line shows a slightly different behaviour, as it does not show the first short temperature increase around 2.5 ms to 3 ms, however the stagnation until the density maximum point is reached with following complete temperature recovery still holds.

The inner divertor shows a different behaviour, see figure 26. First it is denoted that the first two Langmuir probes above the strike line are used, as explained in figure 24. The solid lines are the first and the dashed lines the second LPs above the strike lines. Again the blue line is the odd one out and will be discussed separately. After the ELM again there is a short period around 2 ms with density levels around the pre-ELM values, followed by an increase of density around 2.2 ms. The dashed curves lead one to believe that there are density maxima around 5 ms. However this is due to the strike line movement mentioned earlier. Therefore looking at both LPs combined show an increase of density over a timreange from ~ 2.2 ms (lower fuelling leads to slightly less increase around 4 ms) til around 7 ms to 8 ms and slow decrease til beyond 11 ms.

The temperature evolution shows a hilly structure in between 2.2 ms and 6 ms. After 6 ms the temperature values again are at pre-ELM values.

All in all there is a clear interaction between the electron temperature and density at the outer divertor as well as a dependancy on the deuterium fuelling. However, no obvious electron density-temperature interaction can be seen at the inner divertor as well as no clear inner-outer divertor interaction.

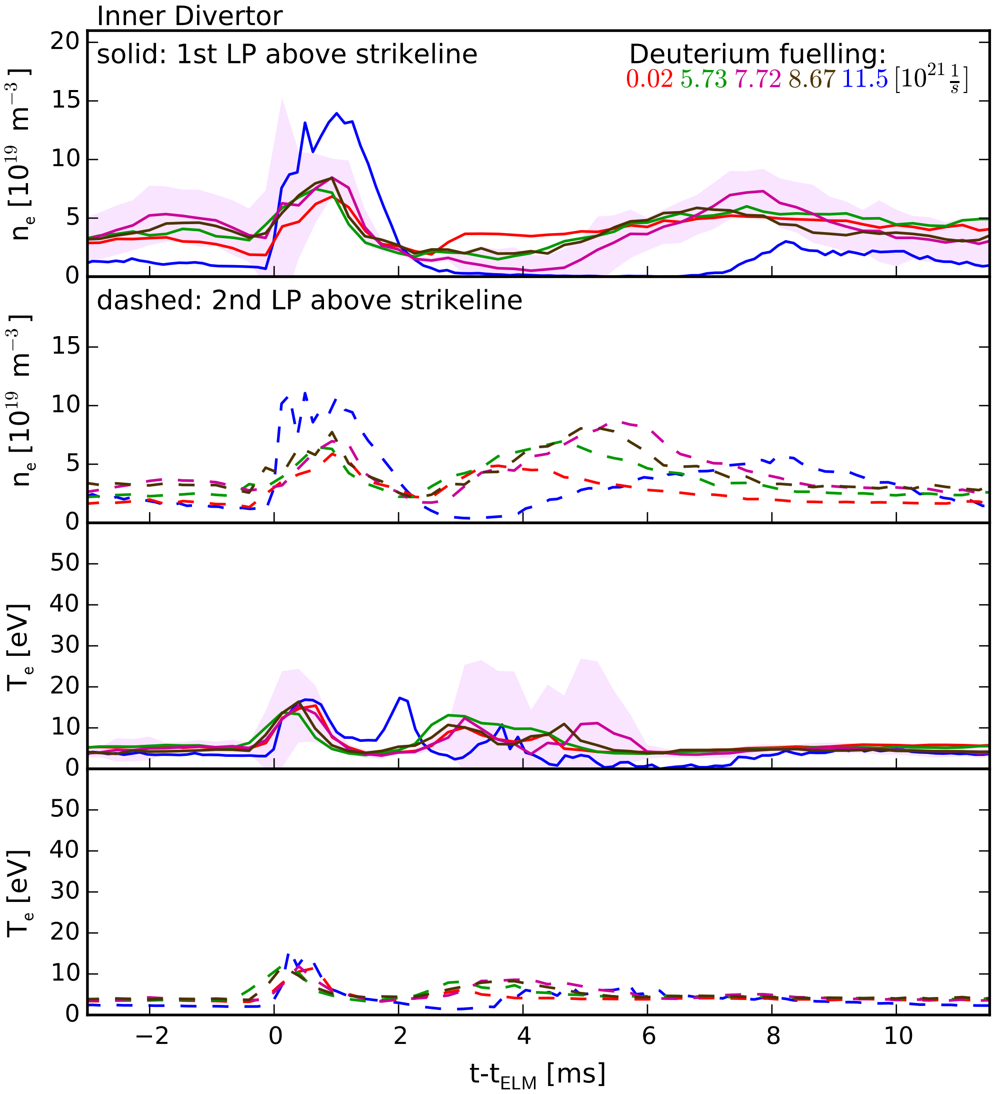

Figure 26: ELM synchronized electron density n_e and temperature T_e evolution at the inner divertor plates for five different deuterium fuelling regimes (red: $0.02 \times 10^{21}\,\frac{1}{\mathrm{s}}$, green: $5.73 \times 10^{21}\,\frac{1}{\mathrm{s}}$, magenta: $7.72 \times 10^{21}\,\frac{1}{\mathrm{s}}$, brown: $8.67 \times 10^{21}\,\frac{1}{\mathrm{s}}$, blue: $11.5 \times 10^{21}\,\frac{1}{\mathrm{s}}$).

4.1.3 Midplane fluctuations

This chapter will characterize the influence of the deuterium fuelling on the midplane fluctuations. The measured data is obtained by superimposing the measurements of the pick-up coils B31-14, B31-03, B31-01, B31-02, B31-12 and B31-13, which are shown in 15. Figure 27 shows the ELM synchronized spectrograms, i.e. midplane fluctuation frequency over time and as third colorbar axes the according intensity. Again the deuterium fuelling scan is presented according to table 2 with increasing fuelling from top to bottom. The intensity is normalized to the maximum of each measurement, therefore each color scaling has different absolute values. Assuming that the maximum intensities, which occur during the ELMs (red color), are similar to each other, it is still possible to obtain useful information.

All of the shot ranges, that differ in the deuterium fuelling rate, show similarities in their magnetic behaviour. The red band at the bottom beneath 15 kHz is due to a mode in the core of the plasma. It is rarely affected by the ELM, which is due to the ELM occurrence only at the plasma edge.

One can see the strong broadband fluctuations at 0 ms during the ELM. As soon as the ELM disappears, a phase of very low midplane magnetic activity sets in at about 1 ms. This region will be called calm or dead phase in the following. Around 4 ms an intense oscillation peak occurs in the vicinity of the core mode frequency, some broadband fluctuations between 20 kHz and 70 kHz, a distinct single band at ∼110 kHz and some less intense fluctuations in the range of 120 kHz to 150 kHz. Around 6 ms the midplane fluctuations become more intense and form distinct single bands with the most intense around 110 kHz.

However, there are also differences. Starting with the pre-ELM phase, it can be seen that with increasing fuelling rate the pre-ELM modes intensity decreases. Furthermore in the dead phase, the onset of the frequency band around 110 kHz to 140 kHz sets in slightly later with increasing fuelling rate. The increasing intensity in the vicinity of 6 ms sets in at slightly different times, but no clear fuelling dependency can be observed.

Due to the increasing ELM frequency and therefore decreasing ELM period, according to table 2, shot range #31513, 2.2 s to 2.6 s and #30701, 2.975 s to 3.4 s show artefacts beyond 10 ms in the ELM synchronization.

Shot range #30701, 2.975 s to 3.4 s shows again further differences. As the ELM lasts longer the dead phase sets in later and the frequency band around 100 kHz to 140 kHz as well. Furthermore it shows a distinct fluctuation increase around 4 ms near the core mode.

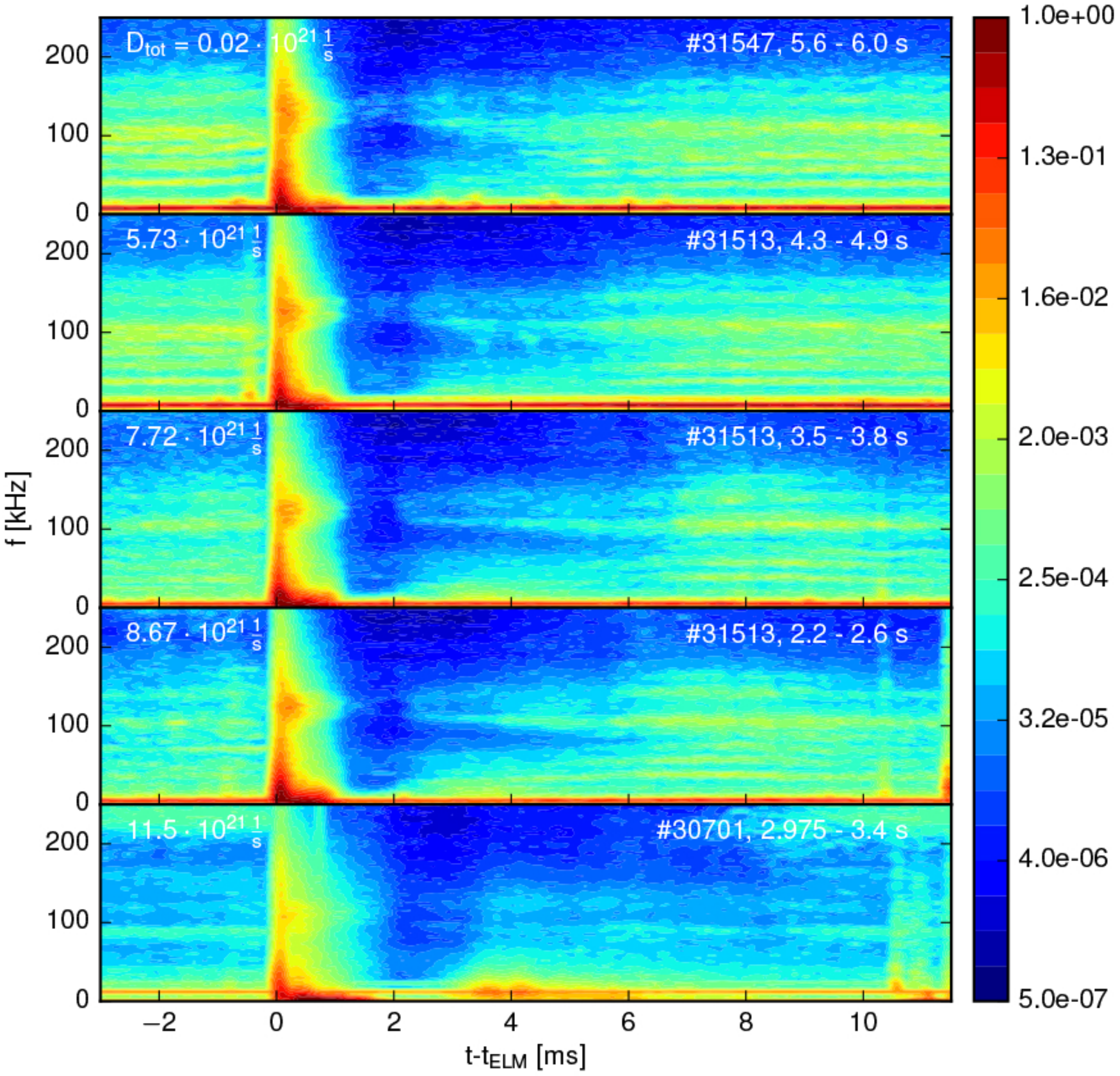

Figure 27: ELM synchronized midplane fluctuations spectrograms. The intensity is normalized to the maximum intensity which occurs during the ELM. Five different deuterium fuelling regimes according to table 2, with increasing fuelling from top to bottom are shown. The data is obtained by superimposing the measurements of the pick-up coils B31-14, B31-03, B31-01, B31-02, B31-12 and B31-13. Their location can be found in figure 15.

4.2 Midplane profiles, midplane fluctuations and divertor relation at the low magnetic field side

In order to understand the inter-ELM edge dynamics it is necessary to look at a combined picture of the inter-ELM evolution of the midplane fluctuations, the midplane profile evolution and the divertor behaviour. As seen in chapter 4.1.2 no clear relation between the inner and outer divertor can be observed, thus the inner divertor inter-ELM evolution will be excluded from the following examinations.
The inter-ELM evolution will be divided into 6 distinct phases in accordance with figure 10 of [26]. The upper plot of figure 28 (#31513, 3.5 s to 3.8 s, $D_{tot} = 7.72 \cdot 10^{21} \frac{1}{s}$) shows the ELM synchronized midplane fluctuation frequency spectrum, below that the electron density (blue) at $\rho_{pol} = 0.98$ and the electron temperature (red) at $\rho_{pol} = 0.94$ of the midplane and at the bottom the density (blue) and temperature (red) at the outer divertor.

Following the pre-ELM phase I, phase II denotes high broadband midplane fluctuations with the ELM onset, a crash in the midplane density and temperature and a peak in the density and temperature at the outer divertor. Phase III indicates a phase of barely any midplane fluctuations, a steep rise of the midplane density together with a rather slow rise of the midplane temperature. At the outer divertor the post-ELM density and temperature dip, followed by a small density shoulder between 2 ms to 3 ms and a short steep increase of the temperature, can be observed. In phase IV midplane fluctuations set in. There is an intense oscillation peak around 4 ms in the vicinity of the core mode frequency, some broadband fluctuations between 20 kHz and 70 kHz, a distinct single band at ~110 kHz and some less intense fluctuations in the range of 120 kHz to 150 kHz. At the same time the density recovery rate decreases, whilst the temperature recovery rate stays constant. The divertor density shows the rise of the second density peak til its maximum is reached at the end of phase IV. During that phase the temperature stays nearly constant. Throughout phase V the midplane fluctuations become more intense and form distinct single bands with the most intense around 110 kHz. The beginning of phase V is characterized by the midplane n_e reaching its maximum value, the density decrease and temperature increase at the divertor. The midplane temperature rises with a slightly increased rate in comparison to phase IV and the divertor temperature reaches its maximum with the maximum intensity of the midplane fluctuations. In phase VI, the midplane fluctuations do not alter and the midplane and divertor density and temperature reach pre-ELM values. Therefore phase VI is treated as equal to phase I.

This related inter-ELM evolution at the low magnetic field side is characteristic for the set of varying deuterium fuelling shot ranges, which is shown in figure 32. Shot (#31513, 3.5 s to 3.8 s, $D_{tot} = 7.72 \cdot 10^{21} \frac{1}{s}$) is already shown in figure 28. There are some deviations of the above mentioned characteristic phases. The $D_{tot} = 0.02 \times 10^{21}\, \frac{1}{\mathrm{s}}$ case shows only the little density hillock, denoted earlier as little density shoulder. Therefore there is no second density peak the midplane density recovery could align with. Additionally the $D_{tot} = 0.02 \times 10^{21}\, \frac{1}{\mathrm{s}}$ case seems to show less magnetic activity in phase IV and V in the range of 40 kHz to 130 kHz, but this is probably due a more pronounced ELM intensity maximum. Furthermore the

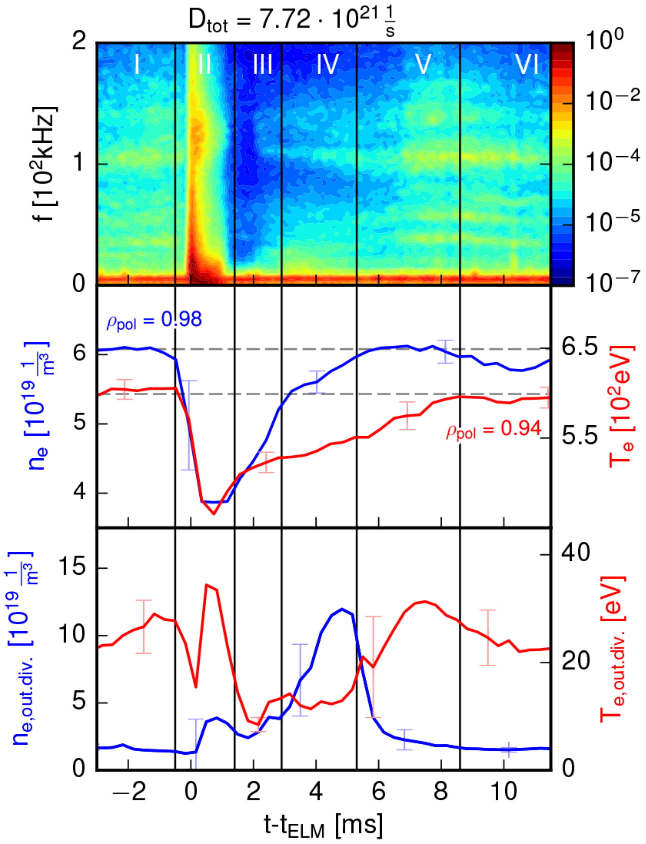

Figure 28: ELM synchronized (top) midplane fluctuation measurements, (center) electron density (blue, $\rho_{pol} = 0.98$) and temperature (red, $\rho_{pol} = 0.94$) at the midplane and (bottom) electron density (blue) and temperature (red) at the outer divertor target (measured by the LP above the strike line). The ELM synchronized evolution is divided into six phases, I-VI. The dashed horizontal lines denote the density and temperature recovery at the midplane.

second density peak is smeared out, however the above described phase evolution still holds.

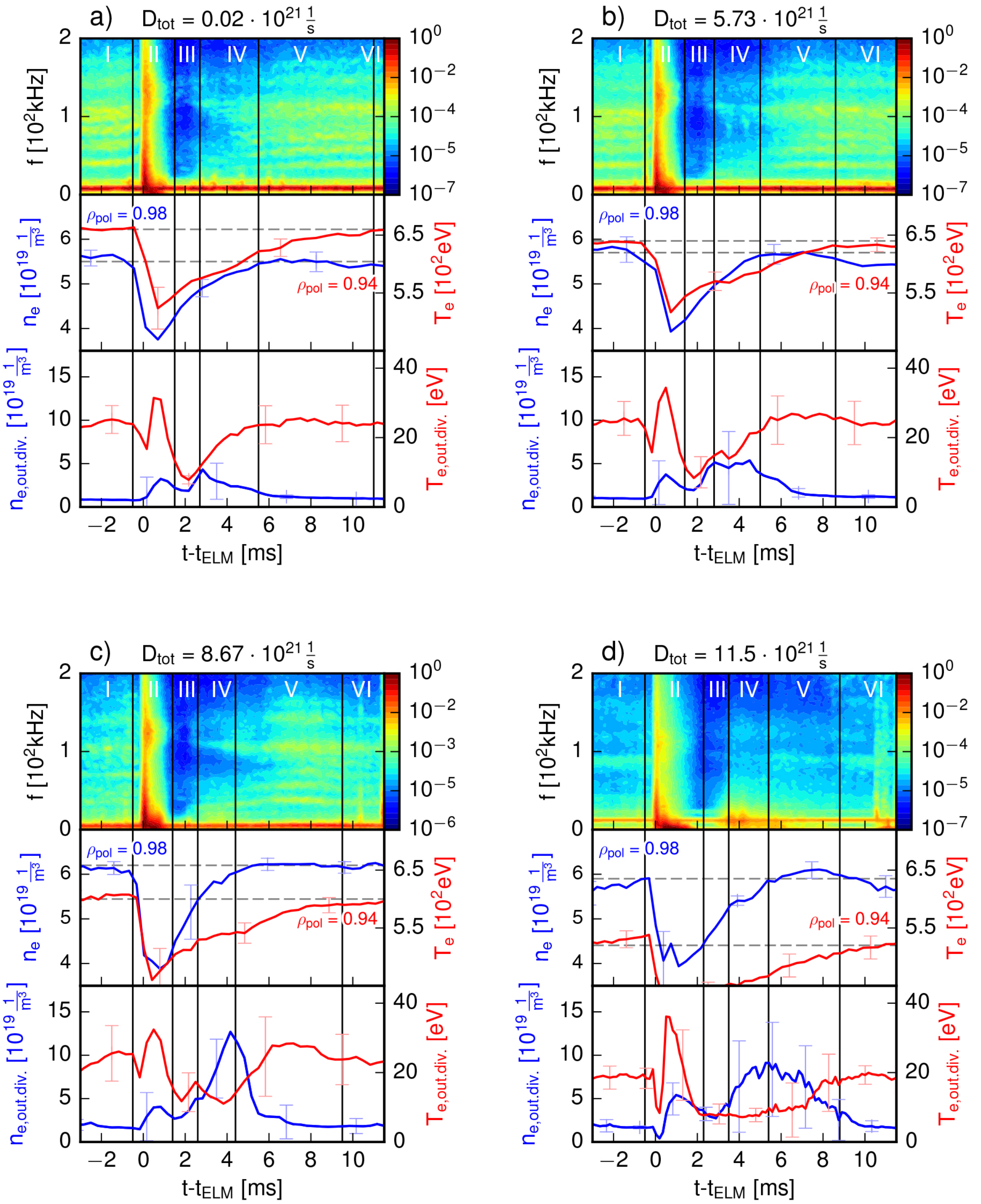

Figure 29: A variety of different fuelling regimes according to table 2. Each shows ELM synchronized (top) midplane fluctuation measurements, (center) electron density (blue) and temperature (red) at the midplane and (bottom) electron density (blue) and temperature (red) at the outer divertor target. The ELM synchronized evolution is divided into six phases, I-VI. The dashed horizontal lines denote the density and temperature recovery at the midplane.

5 Discussion

The observations of chapter 4 will be interpreted in the following chapter 5.1, leading to the conclusion, that the midplane fluctuations are responsible for heat and particle transport into the SOL. Neutrals, originating from the vessel wall, get ionized within the separatrix acting as a counterpart to the midplane fluctuations. The midplane electron density recovery rate is a result of their balance. Chapter 5.2 estimates the additional particle transport due to the midplane fluctuations. Finally, the obtained results are compared to previous investigations.

5.1 Interpretation of the low magnetic field side inter-ELM relation

An attempt to explain these experimental observations obtained in chapter 4.2 will be shown in the following. Figure 30 shows the same as the $D_{tot} = 11.5 \times 10^{21} \, \frac{1}{\mathrm{s}}$ case in figure 32 except that the midplane density scattered data is fitted linearly for $\rho_{pol} = 0.98$, 0.99 and 1.00 for each phase. For each time point t_{III} to t_{VI} the according electron density and temperature profile is shown in figure 31.

After the ELM crash in phase II there is no midplane fluctuation behaviour in phase III. At the same time there is a dip in the density at the divertor. This leads to the assumption that there is only marginal particle transport into the scrape off layer and onto the outer divertor. This phase also shows a rapid rise of the midplane density at $\rho_{pol} = 0.98$ and 0.99. Ions expelled due to an ELM hit the vacuum vessel wall and get neutralized. They can leave the wall either as molecules or atoms with a certain Maxwellian energy distribution. These neutrals fly back through the SOL and mainly get ionized inside the separatrix, acting as a substantial, additional ionization source to the plasma and causing the steep density rise.

In phase IV, the density rise rate decelerates. This is due to the onset of midplane fluctuations, which lead to particle and heat transport outwards and acting as a counterpart to the ionization source. This causes to a reduction of the density rise rate inside the separatrix. At the same time the particle transport due to midplane fluctuations leads to the increase of the second density bump at the outer divertor, whilst the divertor temperature stalls.

Phase V shows an even smaller midplane density rise rate than phase IV. This is due to the decreasing source term. The further increase of the midplane fluctuation intensity leads to more heat transport, causing the rise of the divertor temperature. The even further decreasing source term and the divertor temperature rise result in the divertor density peak decline.

Finally, phase 6 shows that the maximum fluctuation intensity is reached, causing a limit to the divertor temperature rise. Therefore the divertor temperature is again at pre-ELM values. At the same time there is no alteration of the midplane density anymore suggesting that the outward flux and the ionization source due to recycling are in equilibrium.

In summary, the midplane density rise rate is a result of the balance between the outward flux due to midplane fluctuations and the ionization source within the separatrix due to the influx of neutrals.

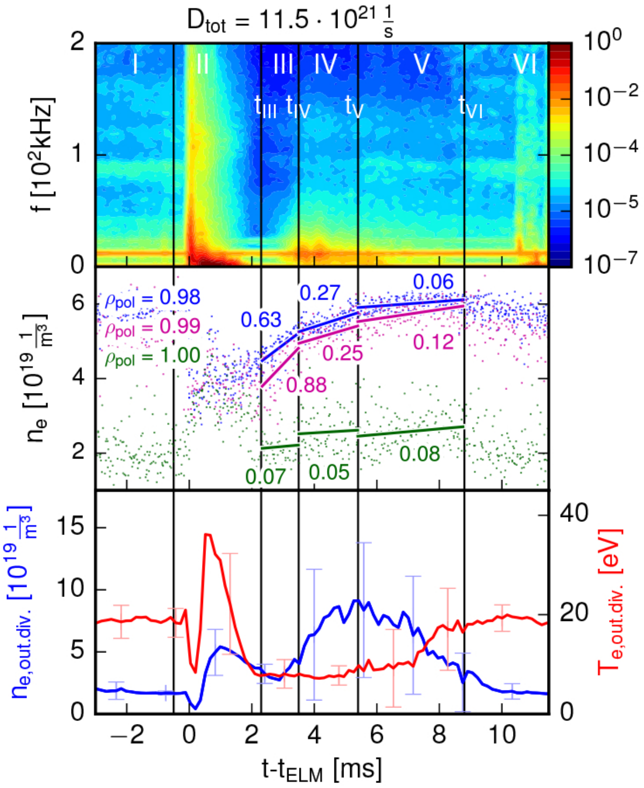

Figure 30: ELM synchronized (top) midplane fluctuation measurements, (center) electron density (blue: $\rho_{pol} = 0.98$, magenta: $\rho_{pol} = 0.99$, green: $\rho_{pol} = 1.00$) at the midplane and (bottom) electron density (blue) and temperature (red) at the outer divertor target (measured by the LP above the strike line). The ELM synchronized evolution is divided into six phases, I-VI. The values in blue, magenta and green denote the electron density rates to each ρ_{pol} and to each phase III-V.

5.2 Additional flux estimation due to midplane fluctuations by using the continuity equation

This behaviour described in the previous chapter can be underpinned by using the flux-surface-averaged particle continuity equation, assuming a drift-diffusion model [68]:

$$\frac{1}{V'}\frac{\partial}{\partial t}(V' n_e) + \frac{1}{V'}\frac{\partial}{\partial \rho_{pol}}\Gamma = \alpha S_i \tag{26}$$

with the volume $V = 2\pi^2\rho^2 R_0$, the volume spatial derivative $\frac{\partial V}{\partial \rho} = V' = 4\pi^2 \rho R_0$, the electron density n_e, the ionization source density rate S_i, a linear factor α and ρ_{pol} the normalized poloidal radius. The particle flux Γ is expressed by:

$$\Gamma = -V' G_1 D \frac{\partial n_e}{\partial \rho} \tag{27}$$

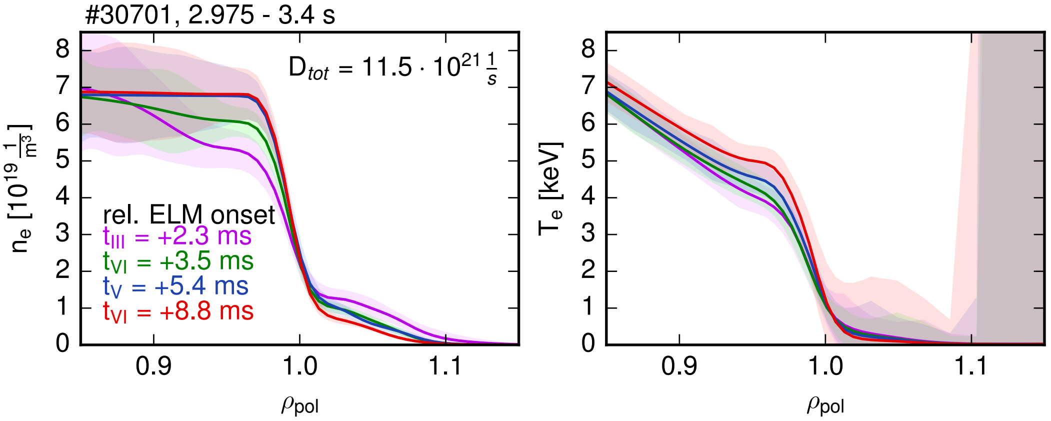

Figure 31: ELM synchronized electron density (left) and temperature (right) versus ρ_{pol} for four time points denoted in figure 30.

$G_1 = \langle(\nabla\rho_{pol})^2\rangle$ denotes the conversion factor from ρ_{pol} space to R space and D the diffusion coefficient.

This equation will be determined for phase III, IV and V. The evaluation of this equation for phase III allows determining the linear factor α in order to estimate the ionization source due to incoming neutrals under the assumption of a flux with a diffusion coefficient of $D = 0.04\frac{m^2}{s}$ [69]. In phase IV and V an additional flux to estimate the particle transport due to midplane fluctuations is introduced. This flux characterization could be either of convective or diffusive nature. In the following the diffusive description is chosen and additional diffusion coefficients D_{IV} and D_V are introduced for phases IV and V, respectively.

Figure 30 shows $\frac{\partial n_e}{\partial t}$ for $\rho_{pol} = 0.98$, 0.99 and 1.00 for shot phase #30701, 2.975 s to 3.4 s. This shot is used as it is the only one with sufficient neutral pressure data. Therefore it is possible to determine the first term to the left of equation 26. The assumption of $D_{III} = 0.04\,\frac{\mathrm{m}^2}{\mathrm{s}}$ and the derivative of n_e in between t_{III} and t_{IV} of figure 31 allows for calculating the particle flux in phase III.

The source term to the right of equation 26 can be modelled by using *KN1D*, which is a 1-D space, 2-D velocity, kinetic transport algorithm. *KN1D* models the neutral atomic and molecular distribution functions, f_n and f_{H_2} in an ionizing plasma. In order to do so background plasma conditions have to be specified: the 1-D geometry dimensions (limiter, SOL and plasma core), the electron density and temperature profile, the ion temperature profile, which is assumed here to be equal to the electron temperature profile and the neutral pressure at the outer midplane vessel wall. Particles leaving the wall are assumed to have a thermal Maxwellian energy distribution.

With these background conditions the plasma-neutral interaction is simulated, based on a numerical algorithm that takes into account charge exchange collisions, electron-impact ionization and dissociation, elastic self-collisions (atomic and molecular), and a variety of elastic cross-collisions [70]. From the modelled distribution functions, several parameters can be derived, as for example the atomic ionization rate S_i.

In this thesis, ELM synchronized electron density and temperature profiles and the ion temperature (set equal to electron temperature) for each time point denoted in figure 31 have been provided for *KN1D*. The electron temperature is approximated with an exponential decay outside the separatrix as the ECE does not provide reliable results in the optically thin region behind the separatrix. Additionally, the deuterium flux density data can be obtained from the neutral pressure gauge 'F17', which is located at the outer midplane vessel wall. The ELM synchronized deuterium flux density is shown in figure 32b. The neutral pressure can be derived from the flux density and the data values according to each time point denoted in figure 31 have been passed on to *KN1D*. The modelled ionization rate profile for each time point relative to the ELM onset can be seen in figure 32a.

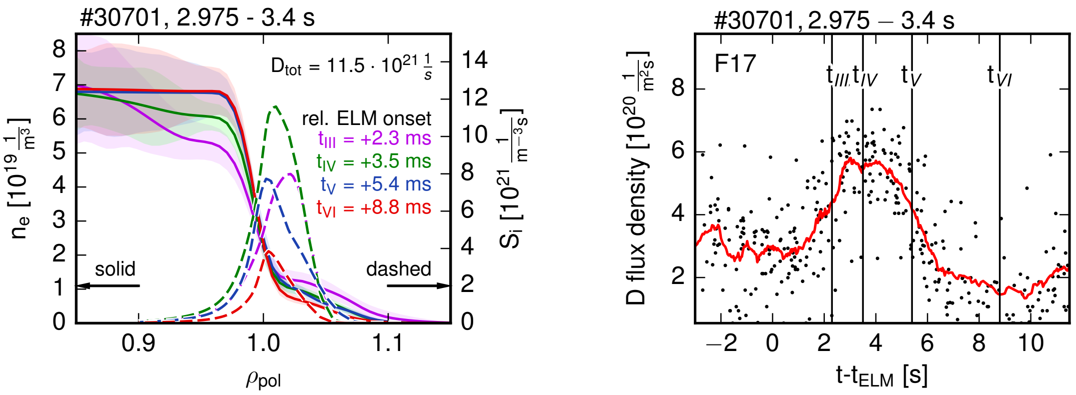

(a) ELM synchronized electron density over ρ_{pol} on the left axis as in the left plot of figure 31. Modelled ionization rate versus ρ_{pol} on the right axis according to each time point t_{III} to t_{VI}.

(b) Scatter data of ELM synchronized deuterium flux density evolution. The red solid line denotes the moving average. Data obtained by the neutral pressure gauge 'F17' (is located at the outer midplane vessel wall).

Figure 32

With these terms of equation 26 determined in dependency of ρ_{pol}, it is possible to estimate the linear factor α averaged over $\rho_{pol} = 0.98$ to $\rho_{pol} = 1.00$ in phase III.

$$\alpha = \frac{\frac{\partial n}{\partial t}_{III} - \frac{D_{III}}{\rho}\langle(\nabla\rho_{pol})^2\rangle\frac{\partial n}{\partial \rho}_{III} - D_{III}\langle(\nabla\rho_{pol})^2\rangle\frac{\partial^2 n}{\partial \rho^2}_{III}}{S_{i,III}} \tag{28}$$

With the constraint to the region between $\rho_{pol} = 0.98$ and $\rho_{pol} = 1.00$ a linear approximation of the electron density profile is valid, seen in the top left figure 33. This leads to the disappearance of the $\frac{\partial^2 n}{\partial \rho^2}_{III}$ term in equation 28. The top right plot of figure 33 shows each term of equation 26 for each phase III, IV and V. The bottom left plot shows the resulting alpha calculation for phase III and its value at $\rho_{pol} = 0.99$.

After having calculated the continuity equation and estimated the linear factor α for the ionization source in phase III, where no midplane fluctuations occur, it is now possible to estimate the additional diffusion coefficients due to the midplane fluctuations in phases IV and V. Equation 29 shows the flux term in phase IV with the additional diffusion constant D_{IV}:

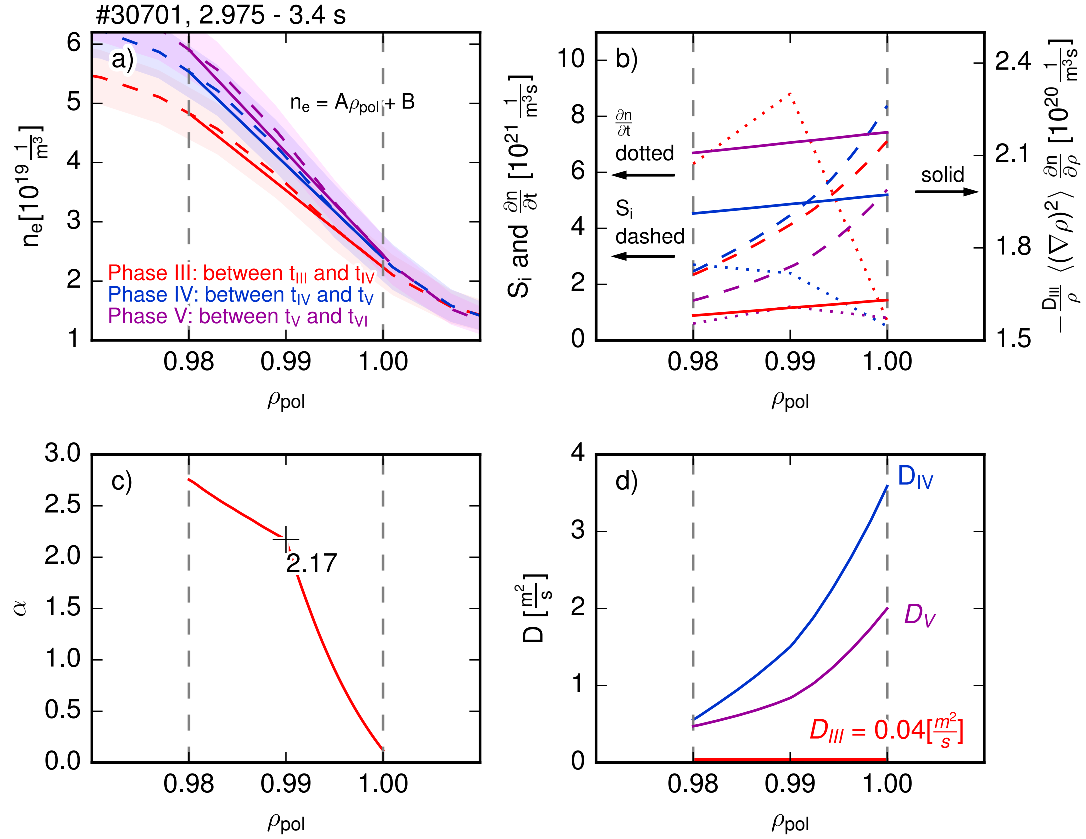

Figure 33: a) ELM synchronized electron density versus ρ_{pol} in between t_{III} and t_{IV}, t_{IV} and t_V and t_V and t_{VI} as dashed lines. The linear approximations are denoted by the solid lines. Plot b) shows the temporal derivative of the electron density as denoted in the center plot of figure 30, which is first upper term of equation 28, the modelled ionization rate S_i (bottom term) and the second upper term of equation 28 versus ρ_{pol}. Plot c) shows the calculation of α according to 28 versus ρ_{pol} and plot d) the estimated total diffusion coefficients D_{IV} and D_V versus ρ_{pol}.

$$\Gamma_{IV} = -V'G_1 D_{III}\frac{\partial n}{\partial \rho}_{IV} - V'G_1 D_{IV}\frac{\partial n}{\partial \rho}_{IV} \tag{29}$$

Equation 30 shows the calculation for the total diffusion coefficient in phase IV, consisting of the diffusion coefficient D_{III} and the additional D_{IV} due to the midplane fluctuations. The result for D_{IV} is shown in the bottom right plot of figure 33:

$$D_{IV,tot} = D_{IV} + D_{III} = \frac{[\frac{\partial n}{\partial t}_{IV} - \alpha S_{i,IV}] - \frac{D_{III}G_1}{\rho}\frac{\partial n}{\partial \rho}_{IV}}{[\frac{G_1}{\rho}\frac{\partial n}{\partial \rho}_{IV}]} + D_{III} \tag{30}$$

The same calculation can be done for phase V leading to the additional diffusion coefficient depicted as well in the bottom right plot of figure 33. Note again, that although a diffusion coefficient is calculated, it does not mean the transport is of diffusive nature. This diffusion coefficient determination should only estimate the ratio between particle transport with and without midplane fluctuations. This first simple estimation shows values for the total diffusion coefficients in phase IV and V of range $0.7\,\frac{\mathrm{m}^2}{\mathrm{s}}$ to $1.5\,\frac{\mathrm{m}^2}{\mathrm{s}}$ for $\rho_{pol} = 0.99$.

5.3 Comparison of the obtained results with previous investigations

The inter-ELM evolution of the outer divertor electron density have been under investigation in [31, 32, 33]. Reference [31] explains the occurrence of the second density peak as a result of local recycling at the outer divertor. However, recycling is not a transient phenomenon and thus can not explain the second density peak transient behaviour nor the time delay of $\sim 8\,\mathrm{ms}$ to the ELM onset, which [31] suggests to explain due to deep deuterium penetration into the divertor surface. Reference [33] gives a short estimation of the flight time of plasma particles in the SOL being $<< 1\,\mathrm{ms}$, in severe discrepancy to the occurrence of the second density peak onset of $\sim 4\,\mathrm{ms}$ or even $\sim 8\,\mathrm{ms}$, seen by [31].

In this thesis, a new model of the second peak evolution is obtained giving an explanation to the above mentioned discrepancies. Simultaneous examination of the electron density and temperature at the outer divertor and at the outer midplane have been conducted revealing their close relation. Furthermore, for the first time ELM synchronized midplane fluctuations with a magnetic signature have been linked to the midplane and divertor inter-ELM evolution. This lead to the concept, that can explain the time delay of the second peak onset due to the later onset of the midplane fluctuations. These fluctuations are responsible for heat and particle transport, that originate in the inner vicinity of the separatrix, as opposed to heat and particle transport from the pedestal top during an ELM crash. This explains why the energy of those particles is below the tungsten sputtering threshold and no second peak in the sputtering flux at the outer divertor can be observed, as seen in [31]. Furthermore, due to the balance of ionization source and particle loss in the pedestal region, no loss in the plasma stored energy W_{mhd} is observed. Additionally, there is no second peak in the impurity flux at the outer divertor, as seen by [31].

In the following chapter the main results of this thesis will be summarized.

6 Summary

The main results of this thesis will be presented in chapter 6.1, followed by a brief outlook in chapter 6.2, that highlights possible improvements to the so far conducted investigation.

6.1 Main results

It is found that the midplane electron density and temperature evolutions are linked to the outer divertor density and temperature evolution. Furthermore, for the first time it has been shown that ELM synchronized midplane fluctuations with a magnetic signature are not only related to the midplane, but also to the outer divertor evolution. A clear relation between the inner and outer divertor inter-ELM evolution could not be identified. The simultaneous examination of the inter-ELM evolution of the midplane pedestal profiles, outer divertor profiles and midplane fluctuations lead to a model, where the density recovery rate can be seen as a result of the interplay of the ionization source due to incoming neutrals originating from the chamber wall and the outgoing particle flux due to particle transport caused by midplane fluctuations. The inter-ELM evolution can be divided into six phases, with the ELM onset in phase II. Phase III shows no midplane fluctuations, thus the density recovery rate is steep due to the large ionization source within the separatrix. In phase IV midplane fluctuations set in, expelling heat and particles into the SOL. Due to that the second density peak in the outer divertor starts rising. Furthermore, the density recovery rate at the midplane decelerates due to the counterpart of the midplane fluctuations to the still strong ionization source. In phase V, the ionization source declines. However the heat transport increases with the intensity of the midplane fluctuations, leading to the rise of the temperature at the outer divertor and the decline of the second density peak. Additionally, the density recovery rate is close to zero showing that the particle outflux and the ionization source are almost in balance, until their equilibrium in phase VI. This new model is capable of describing the relationship of the midplane electron density and temperature, the outer divertor electron density and temperature and the midplane fluctuations and thus is able to explain the mechanism of the second density peak at the outer divertor.
A quantitative estimation of the additional outward transport due to midplane fluctuations is presented in this thesis. By using *KN1D*, a one-dimensional transport algorithm for atomic and molecular hydrogen in an ionizing plasma, the ionization source due to a neutral influx can be modelled. This neutral flux is due to recycling from PFCs, which is rising shortly after an ELM due to particles that have been expelled by an ELM as ions. Applying the drift-diffusion model based continuity equation for phase III,IV and V, respectively, leads to the evaluation of a linear factor α that estimates the particle source in phase III and the estimation of diffusion coefficients of the order of $0.7\,\frac{\mathrm{m}^2}{\mathrm{s}}$ to $1.5\,\frac{\mathrm{m}^2}{\mathrm{s}}$ due to additional transport of the midplane fluctuations in phases IV and V.

6.2 Future perspectives

A plasma discharge with a continuous increase of deuterium fuelling could be performed in order to investigate the continuous dependency of the inter-ELM evolution at the divertor and midplane on the deuterium fuelling. This should be performed while keeping a constant plasma current, toroidal magnetic field, total heating power and plasma geometry.

Furthermore the ionization profile modelling can be improved by using a Maxwellian velocity distribution with higher mean velocity in addition to the so far used thermal distribution, in order to take into account the higher particle and energy reflection coefficients of deuterium reflected from a tungsten wall. Additionally, the heat and particle transport estimation could be performed using *ASTRA* [68], an automated system for transport analysis in a tokamak.

A Acknowledgement

Obwohl die Danksagung keine physikalischen Gedankengänge erfordert, ist sie dennoch von allen Kapiteln am schwierigsten zu schreiben, da man den Menschen, die mit an dieser Arbeit beteiligt waren, nie genügend danken kann.

Mein besonderer Dank geht an:
Meinen Betreuer Friedrich Aumayr, der mir diese Arbeit überhaupt ermöglicht hat. Durch ihn wurde der Kontakt an das Max-Planck-Institut für Plasmaphysik in Garching hergestellt und des Weiteren wurden alle Forschungsaufenthalte von ihm finanziell unterstützt.
Meine Betreuerin Elisabeth Wolfrum, die mich sehr herzlich in ihrer Arbeitsgruppe am IPP aufgenommen hat und mir stets den richtigen Weg gezeigt hat. Ihre unaufhaltsame Begeisterung für die Physik und gleichzeitige Begabung diese an junge Physiker weiterzugeben, war sehr inspirierend und hat mich nachhaltig positiv geprägt.
Meinen Co-Betreuer Florian Laggner, der durchwegs Antworten auf die alltäglichen Fragen eines Kernfusionsneulings parat hatte und sehr viel Zeit und Geduld für mich aufgebracht hat.
Felician Mink für die freundliche Bereitstellung seiner Plot-Routinen und Antworten meiner Fragen bezüglich der magnetischen Oszillationen. Steffen Potzel für die Bereitstellung des Divertor-Programms und Matthias Bernert für den KN1D Transportcode.
Meinen Bürokollegen in Garching, die stets für ein Abendbier zur Verfügung standen, vor allem meine Kollegen Sergiu und Jakob.
Meinen Bürokollegen in Wien, die stets für gute Laune während der Arbeit gesorgt haben.
Meinen langjährigen Physikerfreunden, die während all der Jahre in guten wie auch schlechten Zeiten zu mir standen. Danke Jason, Sigrid, Jakob, Gregor, Daniel und Adrian. Danke auch an meine Lieblingsmitbewohnerin Bella für die Geduld mit mir, vorallem in der letzten Zeit.

Mein ganz besonderer Dank geht an meine Familie, besonders an meine Eltern, die ausnahmslos die ganze Zeit meines Lebens an mich geglaubt haben und immer die Grundpfeiler meines Lebens waren und sein werden. Außerdem an meinen Bruder, der sich sicher seinen eigenen, interessanten Weg in der Physik bahnen wird.
The best comes last. Thank you Kasia, my beautiful girlfriend, for proofreading my thesis and being so supportive and understanding in everything I did in the last three years!

B List of Figures

1 Time series (1850-2300) of global annual mean surface air temperature changes (taken from the *Coupled Model Intercomparison Project Phase 5* concentration-driven experiments). Projections are shown for four *representative concentration pathways* (RCP) for the multi-model mean (solid lines) and ±1.64 standard deviation (5 to 95%) across the distribution of individual models (shading), based on annual means. This shows that according to four different CO_2 emission progressions, the global surface temperature can reach levels of 1 °C, 2 °C, 2.5 °C, 4 °C by the end of the century in addition to the global temperature nowerdays [2]. 2

2 Binding energy per nucleon $\frac{B}{A}$ over nucleon number A [5]. 3

3 Cross sections for several fusion reactions versus the energy of deuterium. The D-T fusion reaction ($T(d,n)^4He$) has a significantly higher cross section at lower energies than the D-D ($D(d,n)^3He$) or the D-^3He ($^3He(d,n)^4He$) reaction. Figure taken from [6] with data from [7, 8]. 4

4 Magnetic fusion concepts 5

5 The *ITER* experiment is a Tokomak whose geometry takes its lead from the Garching machine *ASDEX Upgrade* – albeit four times larger (notice the little man to the bottom right)[12]. 7

6 Radial pressure profiles versus minor radius for L-mode (black, dashed) and H-mode (red, solid). In H-mode an edge transport barrier leads to steep edge gradients called the pedestal. [14]. 8

7 Typical edge localized mode (ELM) cycle in a poloidal cross section and its corresponding pressure profile progression [16]. 9

8 Bootstrap current versus pressure gradient. Typical ELM cycles, according to each type, are shown in this peeling-ballooning stability diagram [20]. 9

9 (a) Temperature gradient and (b) density gradient evolution relative to the ELM onset. This evolution is divided into six phases: phase I (blue), phase II (yellow), phase III (red), phase IV (green), phase V (magenta) and phase VI (grey) [26]. 12

10 ELM resolved edge current density versus normalized edge pressure gradient. Operational points denoted by stars, peeling-ballooning stability boundaries by curves (color codes as in figure 9) [26]. 12

11 ELM time averaged (a) total impinging ion flux measured by Langmuir Probes, (b) total D_α photon flux as marker for recycling, (c) photon flux resulting from impinging Be ions (BeII at 527.1 nm), and (d) photon flux of sputtered W atoms from the bulk-W divertor PFCs (WI at 400.9 nm) [31]. 14

12 Coherent ELM averaged signals of (a) the D_α time trace and the outer target profiles for three distinct time slices during the second D_α peak: (b) power deposition profiles from IR, (c) particle flux and (d) T_e measured with Langmuir Probes. [33]. 15

13 ELM-synchronised spectrogram of $\frac{\partial B_r}{\partial t}$ and ELM-synchronised time traces of $\max(\nabla n_e)$ (blue), $\max(\nabla T_e)$ (red) and inner divertor current (black) for the a) low collisionality case and b) high collisionality case. [35]. 17

14 Inter-ELM magnetic fluctuations spectrograms showing the QCFs in low (a) and high (b) current cases. The shaded areas on the spectrograms represent the core modes and broadband fluctuations which are not ELM related events. The QCF amplitude's evolution relative to the ELM onset for the frequency bands (c) 23 kHz to 60 kHz and (d) 120 kHz to 170 kHz is shown together with the temperature gradient evolutions. [37]. 18

15 Toroidal (left) and poloidal (right) cross sections of the *ASDEX Upgrade* Tokamak vessel. The diagnostics are shown in different colors: Lithium beam (magenta), electron cyclotron emission diagnostic (green), deuterium cyanide laser (red), pick up coils (brown), Stark broadening diagnostic (orange), Thomson scattering (blue) and the Langmuir probes (cyan). The LPs are not shown in the toroidal cross section. 21

16 Schematic sketch of the Lithium beam emission spectroscopy setup [49]. 22

17 Spectral distribution of scattered power from a Nd:YAG laser [55] . . 24

18 Deuterium cyanide laser interferometry sketch [59] 26

19 Schematic comparison of the (a) conventional data analysis with the (b) IDA approach [60]. 27

20 Spectral radiance versus wavelength. Example fit to the D_ϵ line yielding n_e [63]. 29

21 Theoretical current-voltage characteristic of a Langmuir probe. All potentials denoted here are relative to the vessel potential [66]. 30

22 ELM synchronized density ($\rho_{pol} = 0.98$ and $\rho_{pol} = 1.01$) and temperature ($\rho_{pol} = 0.94$) evolutions at the outer midplane for different deuterium fuelling regimes (red: $0.02 \times 10^{21}\,\frac{1}{\mathrm{s}}$, green: $5.73 \times 10^{21}\,\frac{1}{\mathrm{s}}$, magenta: $7.72 \times 10^{21}\,\frac{1}{\mathrm{s}}$, brown: $8.67 \times 10^{21}\,\frac{1}{\mathrm{s}}$, blue: $11.5 \times 10^{21}\,\frac{1}{\mathrm{s}}$) . . 34

23 ELM synchronized electron density n_e and temperature T_e evolution at the inner (left) and the outer (right) divertor plates for shot 31513 in the time range of 3.5 s to 3.8 s. The magenta continuous line denotes the moving average of the scattered data. Note that not all data points are shown in the inner divertor density plot, as a few data points scattered up to values of $130 \times 10^{19}\,\frac{1}{\mathrm{m}^3}$. 35

24 On the left: Single ELM density evolution at 4 different Langmuir probes at each divertor plate for shot 31513. Langmuir probes at the outer divertor are denoted by ua3: green, ua4: red, ua5: blue, ua6: magenta and at the inner divertor ui5: magenta, ui6: green, ui7: red, ui8: blue. On the right: Enlarged poloidal cross section of the outer (top) and inner (bottom) divertor plates with the color coded Langmuir probes. The black continuous line denotes the separatrix (strikeline) at the time point 3.612 s, the dashed line at 3.613 s, the dotted line at 3.615 s and the dashed-dotted line at 3.617 s. 36

25 ELM synchronized electron density n_e and temperature T_e evolution at the outer divertor plates for five different deuterium fuelling regimes (red: $0.02 \times 10^{21}\,\frac{1}{\mathrm{s}}$, green: $5.73 \times 10^{21}\,\frac{1}{\mathrm{s}}$, magenta: $7.72 \times 10^{21}\,\frac{1}{\mathrm{s}}$, brown: $8.67 \times 10^{21}\,\frac{1}{\mathrm{s}}$, blue: $11.5 \times 10^{21}\,\frac{1}{\mathrm{s}}$). The light magenta shaded area denotes the standard deviation to the magenta line. 37

26 ELM synchronized electron density n_e and temperature T_e evolution at the inner divertor plates for five different deuterium fuelling regimes (red: $0.02 \times 10^{21}\,\frac{1}{\mathrm{s}}$, green: $5.73 \times 10^{21}\,\frac{1}{\mathrm{s}}$, magenta: $7.72 \times 10^{21}\,\frac{1}{\mathrm{s}}$, brown: $8.67 \times 10^{21}\,\frac{1}{\mathrm{s}}$, blue: $11.5 \times 10^{21}\,\frac{1}{\mathrm{s}}$). 39

27 ELM synchronized midplane fluctuations spectrograms. The intensity is normalized to the maximum intensity which occurs during the ELM. Five different deuterium fuelling regimes according to table 2, with increasing fuelling from top to bottom are shown. The data is obtained by superimposing the measurements of the pick-up coils B31-14, B31-03, B31-01, B31-02, B31-12 and B31-13. Their location can be found in figure 15. 41

28 ELM synchronized (top) midplane fluctuation measurements, (center) electron density (blue, $\rho_{pol} = 0.98$) and temperature (red, $\rho_{pol} = 0.94$) at the midplane and (bottom) electron density (blue) and temperature (red) at the outer divertor target (measured by the LP above the strike line). The ELM synchronized evolution is divided into six phases, I-VI. The dashed horizontal lines denote the density and temperature recovery at the midplane. 43

29 A variety of different fuelling regimes according to table 2. Each shows ELM synchronized (top) midplane fluctuation measurements, (center) electron density (blue) and temperature (red) at the midplane and (bottom) electron density (blue) and temperature (red) at the outer divertor target. The ELM synchronized evolution is divided into six phases, I-VI. The dashed horizontal lines denote the density and temperature recovery at the midplane. 44

30 ELM synchronized (top) midplane fluctuation measurements, (center) electron density (blue: $\rho_{pol} = 0.98$, magenta: $\rho_{pol} = 0.99$, green: $\rho_{pol} = 1.00$) at the midplane and (bottom) electron density (blue) and temperature (red) at the outer divertor target (measured by the LP above the strike line). The ELM synchronized evolution is divided into six phases, I-VI. The values in blue, magenta and green denote the electron density rates to each ρ_{pol} and to each phase III-V. 46

31 ELM synchronized electron density (left) and temperature (right) versus ρ_{pol} for four time points denoted in figure 30. 47
32 48
33 a) ELM synchronized electron density versus ρ_{pol} in between t_{III} and t_{IV}, t_{IV} and t_V and t_V and t_{VI} as dashed lines. The linear approximations are denoted by the solid lines. Plot b) shows the temporal derivative of the electron density as denoted in the center plot of figure 30, which is first upper term of equation 28, the modelled ionization rate S_i (bottom term) and the second upper term of equation 28 versus ρ_{pol}. Plot c) shows the calculation of α according to 28 versus ρ_{pol} and plot d) the estimated total diffusion coefficients D_{IV} and D_V versus ρ_{pol}. 49

C Bibliography

[1] REN21. *Fossil fuel based energy share of global final energy consumption, 2013.* `http://www.ren21.net/wp-content/uploads/2015/07/GSR2015_KeyFindings_lowres.pdf` (2015). [Online; accessed 8-April-2016].

[2] IPCC. *Time series of global annual mean surface air temperature anomalies (relative to 1986–2005) from CMIP5 concentration-driven experiments.* `https://www.ipcc.ch/pdf/assessment-report/ar5/wg1/WG1AR5_SummaryVolume_FINAL.pdf` (2013). [Online; accessed 8-April-2016].

[3] K. Yoshihara. *Technetium in the environment.* In *Technetium and Rhenium: Their Chemistry and Its Applications*, pp. 17–35. Springer (1996).

[4] J. Ongena and G. Van Oost. *Energy for future centuries. Will fusion be an inexhaustible, safe and clean energy source?* Fusion Technology **37** (2000).

[5] L. Sitton. *Binding energy per nucleon.* `http://staff.orecity.k12.or.us/les.sitton/Nuclear/313_files/nfg005.gif` (2007). [Online; accessed 15-March-2016].

[6] F. Laggner. *Electron Density Perturbations at the Plasma Edge of the ASDEX Upgrade Tokamak.* Master thesis, Institut für Angewandte Physik, TU Wien (2013).

[7] G. H. Miley, H. Towner, and N. Ivich. *Fusion cross sections and reactivities.* Tech. rep., Illinois Univ., Urbana (USA) (1974).

[8] H. S. Bosch and G. M. Hale. *Improved formulas for fusion cross-sections and thermal reactivities.* Nuclear Fusion **32**, 611 (1992).

[9] EUROfusion. *Tokamak Principle.* `https://www.euro-fusion.org/2011/09/tokamak-principle-2/` (2011). [Online; accessed 14-March-2016].

[10] C. Bickel and IPP. *Tokamak Principle.* `http://i.dailymail.co.uk/i/pix/2015/10/26/17/2DCE762200000578-0-image-a-1_1445880883149.jpg` (2015). [Online; accessed 15-March-2016].

[11] H. Zohm and the EUROfusion MST1 Team. *Recent ASDEX Upgrade research in support of ITER and DEMO.* Nuclear Fusion **55**, 104010 (2015).

[12] ITER. *ITER Principle.* `http://www.ipp.mpg.de/16617/iter` (2015). [Online; accessed 15-March-2016].

[13] F. Wagner. *A quarter-century of H-mode studies.* Plasma Physics and Controlled Fusion **49**, B1 (2007).

[14] Wikifusion. *H-mode.* `http://images.google.de/imgres?imgurl=http%3A%2F%2Fwiki.fusenet.eu%2Ffusionwiki%2Fimages%2Fthumb%2Fa%2Fa6%2FH-mode.png%2F300px-H-mode.png&imgrefurl=http%3A%2F%2Fwiki.fusenet.eu%2Ffusionwiki%2Findex.php%2FPedestal&h=302&w=300&tbnid=aRv68kUu2TkO_M%3A&docid=XcbqP2tB3sIDeM&ei=RvgMV_6jFIjOa6KFmJAE&tbm=isch&iact=rc&uact=3&page=1&start=0&ndsp=27&ved=0ahUKEwj-3vy6monMAhUI5xoKHaICBkIQMwgfKAEwAQ` (2011). [Online; accessed 12-April-2016].

[15] E. Viezzer, T. Pütterich, G. Conway, R. Dux, T. Happel, J. Fuchs, R. McDermott, F. Ryter, B. Sieglin, W. Suttrop *et al. High-accuracy characterization of the edge radial electric field at ASDEX Upgrade.* Nuclear Fusion **53**, 053005 (2013).

[16] EUROfusion. *Time development of an ELM crash.* `https://www.euro-fusion.org/wpcms/wp-content/uploads/2011/07/fig12.jpg` (2015). [Online; accessed 23-March-2016].

[17] D. Dickinson, C. Roach, S. Saarelma, R. Scannell, A. Kirk, and H. Wilson. *Kinetic instabilities that limit β in the edge of a tokamak plasma: a picture of an H-mode pedestal.* Physical Review Letters **108**, 135002 (2012).

[18] J. Connor, R. Hastie, H. Wilson, and R. Miller. *Magnetohydrodynamic stability of tokamak edge plasmas.* Physics of Plasmas **5**, 2687 (1998).

[19] P. Snyder, H. Wilson, J. Ferron, L. Lao, A. Leonard, T. Osborne, A. Turnbull, D. Mossessian, M. Murakami, and X. Xu. *Edge localized modes and the pedestal: a model based on coupled peeling–ballooning modes.* Physics of Plasmas (1994-present) **9**, 2037 (2002).

[20] S. Rathgeber. *Electron temperature and pressure at the edge of ASDEX Upgrade plasmas.* Phd thesis, Fakultät für Physik, LMU München (2013).

[21] H. Zohm. *Edge localized modes (ELMs).* Plasma Physics and Controlled Fusion **38**, 105 (1996).

[22] E. Wolfrum, M. Bernert, J. Boom, A. Burckhart, I. Classen, G. Conway, T. Eich, R. Fischer, A. Gude, A. Herrmann *et al. Characterization of edge profiles and fluctuations in discharges with type-II and nitrogen-mitigated edge localized modes in ASDEX Upgrade.* Plasma Physics and Controlled Fusion **53**, 085026 (2011).

[23] W. Suttrop. *The physics of large and small edge localized modes.* Plasma Physics and Controlled Fusion **42**, A1 (2000).

[24] T. Luce. *An analytic functional form for characterization and generation of axisymmetric plasma boundaries.* Plasma Physics and Controlled Fusion **55**, 095009 (2013).

[25] A. Burckhart, E. Wolfrum, R. Fischer, K. Lackner, H. Zohm *et al.* *Inter-ELM behaviour of the electron density and temperature pedestal in ASDEX Upgrade.* Plasma Physics and Controlled Fusion **52**, 105010 (2010).

[26] E. Wolfrum, E. Viezzer, A. Burckhart, M. Dunne, P. Schneider, M. Willensdorfer, E. Fable, R. Fischer, D. Hatch, F. Jenko *et al.* *Overview of recent pedestal studies at ASDEX Upgrade.* Nuclear Fusion **55**, 053017 (2015).

[27] A. Burckhart. *Different ELM regimes at ASDEX Upgrade and their linear stability analysis.* Phd thesis, Fakultät für Physik, LMU München (2013).

[28] D. Hatch, D. Told, F. Jenko, H. Doerk, M. Dunne, E. Wolfrum, E. Viezzer, M. Pueschel *et al.* *Gyrokinetic study of ASDEX Upgrade inter-ELM pedestal profile evolution.* Nuclear Fusion **55**, 063028 (2015).

[29] F. Jenko, W. Dorland, M. Kotschenreuther, and B. Rogers. *Electron temperature gradient driven turbulence.* Physics of Plasmas (1994-present) **7**, 1904 (2000).

[30] R. Groebner, P. Snyder, T. Osborne, A. Leonard, T. Rhodes, L. Zeng, E. A. Unterberg, Z. Yan, G. McKee, C. Lasnier *et al.* *Limits to the H-mode pedestal pressure gradient in DIII-D.* Nuclear Fusion **50**, 064002 (2010).

[31] S. Brezinsek, S. Wiesen, D. Harting, C. Guillemaut, A. Webster, K. Heinola, A. Meigs, M. Rack, Y. Gao, G. Sergienko *et al.* *Characterisation of the deuterium recycling at the W divertor target plates in JET during steady-state plasma conditions and ELMs.* Physica Scripta **2016**, 014076 (2016).

[32] A. Y. Pigarov, S. Krasheninnikov, T. Rognlien, E. Hollmann, C. Lasnier, and E. Unterberg. *Multi-fluid transport code modeling of time-dependent recycling in ELMy H-mode.* Physics of Plasmas (1994-present) **21**, 062514 (2014).

[33] M. Wischmeier, A. Kallenbach, A. Chankin, D. Coster, T. Eich, A. Herrmann, H. Müller, and A. U. Team. *High recycling outer divertor regimes after type-I ELMs at high density in ASDEX Upgrade.* Journal of Nuclear Materials **363**, 448 (2007).

[34] J. Stober, P. Lomas, G. Saibene, Y. Andrew, P. Belo, G. Conway, A. Herrmann, L. Horton, M. Kempenaars, H.-R. Koslowski *et al.* *Small ELM regimes with good confinement on JET and comparison to those on ASDEX Upgrade, Alcator C-mod and JT-60U.* Nuclear Fusion **45**, 1213 (2005).

[35] F. Laggner, E. Wolfrum, M. Cavedon, F. Mink, E. Viezzer, M. G. Dunne, P. Manz, H. Doerk, G. Birkenmeier, R. Fischer, S. Fietz, M. Maraschek, M. Willensdorfer, F. Aumayr, the EUROfusion MST1 Team, and the ASDEX Upgrade Team. *High frequency magnetic fluctuations correlated with the inter-ELM pedestal evolution in ASDEX Upgrade.* Submitted, 2016.

[36] T. Bolzonella, H. Zohm, M. Maraschek, E. Martines, S. Saarelma, S. Günter, and A. U. Team. *High frequency MHD activity related to type I ELMs in ASDEX Upgrade.* Plasma Physics and Controlled Fusion **46**, A143 (2004).

[37] A. Diallo, R. Groebner, T. Rhodes, D. Battaglia, D. Smith, T. Osborne, J. Canik, W. Guttenfelder, and P. Snyder. *Correlations between quasi-coherent fluctuations and the pedestal evolution during the inter-edge localized modes phase on DIII-D.* Physics of Plasmas (1994-present) **22**, 056111 (2015).

[38] A. Diallo, J. Hughes, M. Greenwald, B. LaBombard, E. Davis, S. Baek, C. Theiler, P. Snyder, J. Canik, J. Walk *et al. Observation of edge instability limiting the pedestal growth in tokamak plasmas.* Physical review letters **112**, 115001 (2014).

[39] A. Diallo, J. Hughes, S. Baek, B. LaBombard, J. Terry, I. Cziegler, A. Hubbard, E. Davis, J. Walk, L. Delgado-Aparicio *et al. Quasi-coherent fluctuations limiting the pedestal growth on Alcator C-Mod: experiment and modelling.* Nuclear Fusion **55**, 053003 (2015).

[40] C. Perez, H. Koslowski, T. Hender, P. Smeulders, A. Loarte, P. Lomas, G. Saibene, R. Sartori, M. Becoulet, T. Eich *et al. Washboard modes as ELM-related events in JET.* Plasma Physics and Controlled Fusion **46**, 61 (2003).

[41] F. Aumayr and H. Winter. *Plasmadiagnostik mit Lithiumatomstrahl-aktivierter Umladungsspektroskopie.* Annalen der Physik **497**, 228 (1985).

[42] E. Wolfrum, F. Aumayr, D. Wutte, H. Winter, E. Hintz, D. Rusbüldt, and R. Schorn. *Fast lithium-beam spectroscopy of tokamak edge plasmas.* Review of Scientific Instruments **64**, 2285 (1993).

[43] J. Schweinzer, E. Wolfrum, F. Aumayr, M. Pockl, H. Winter, R. Schorn, E. Hintz, and A. Unterreiter. *Reconstruction of plasma edge density profiles from Li I (2s-2p) emission profiles.* Plasma Physics and Controlled Fusion **34**, 1173 (1992).

[44] D. Thomas, A. Hyatt, and M. Thomas. *Edge density fluctuation diagnostic for DIII-D using lithium beams.* Review of Scientific Instruments **61**, 3040 (1990).

[45] R. Schorn, E. Hintz, D. Rusbüldt, F. Aumayr, M. Schneider, E. Unterreiter, and H. Winter. *Absolute concentrations of light impurity ions in tokamak discharges measured with lithium-beam-activated charge-exchange spectroscopy.* Applied Physics B **52**, 71 (1991).

[46] S. Fiedler, R. Brandenburg, J. Baldzuhn, K. McCormick, F. Aumayr, J. Schweinzer, H. Winter *et al. Edge plasma diagnostics on W7-AS and ASDEX-Upgrade using fast Li beams.* Journal of Nuclear Materials **266**, 1279 (1999).

[47] R. Brandenburg, J. Schweinzer, S. Fiedler, F. Aumayr, and H. Winter. *Modelling of fast neutral Li beams for fusion edge plasma diagnostics.* Plasma Physics and Controlled Fusion **41**, 471 (1999).

[48] R. Brandenburg, F. Aumayr, H. Winter, G. Petravich, S. Zoletnik, S. Fiedler, K. McCormick, and J. Schweinzer. *Fast lithium beam edge plasma spectroscopy*

at IPP Garching: Status and recent developments. Fusion Technology **36**, 289 (1999).

[49] M. Willensdorfer, E. Wolfrum, R. Fischer, J. Schweinzer, M. Sertoli, B. Sieglin, G. Veres, F. Aumayr *et al. Improved chopping of a lithium beam for plasma edge diagnostic at ASDEX Upgrade.* Review of Scientific Instruments **83**, 023501 (2012).

[50] R. Fischer, E. Wolfrum, J. Schweinzer *et al. Probabilistic lithium beam data analysis.* Plasma Physics and Controlled Fusion **50**, 085009 (2008).

[51] M. Willensdorfer. *Temporal behaviour of the plasma edge density throughout the L-H transition in ASDEX Upgrade.* Phd thesis, Institut für Angewandte Physik, TU Wien (2013).

[52] M. Willensdorfer, G. Birkenmeier, R. Fischer, F. Laggner, E. Wolfrum, G. Veres, F. Aumayr, D. Carralero, L. Guimarãis, B. Kurzan *et al. Characterization of the Li-BES at ASDEX Upgrade.* Plasma Physics and Controlled Fusion **56**, 025008 (2014).

[53] W. Suttrop. *Electron cyclotron emission plasma diagnostics.* `http://www.aug.ipp.mpg.de/aug/local/diagnostik4/ece/eceprinciple.pdf` (2009). [Online; accessed 24-March-2016].

[54] S. Rathgeber, L. Barrera, T. Eich, R. Fischer, B. Nold, W. Suttrop, M. Willensdorfer, E. Wolfrum *et al. Estimation of edge electron temperature profiles via forward modelling of the electron cyclotron radiation transport at ASDEX Upgrade.* Plasma Physics and Controlled Fusion **55**, 025004 (2012).

[55] R. Scannel. *Investigation of H-mode edge profile behaviour on MAST using Thomson scattering.* Phd thesis, Department of Physics, University College Cork (2007).

[56] E. E. Salpeter. *Electron density fluctuations in a plasma.* Physical Review **120**, 1528 (1960).

[57] N. Peacock, D. Robinson, M. Forrest, P. Wilcock, and V. Sannikov. *Measurement of the electron temperature by Thomson scattering in tokamak T3.* Nature **224**, 448 (1969).

[58] H. Murmann, S. Götsch, H. Röhr, H. Salzmann, and K. Steuer. *The Thomson scattering systems of the ASDEX Upgrade tokamak.* Review of Scientific Instruments **63**, 4941 (1992).

[59] E. T. Demichlis, C. *Tokamak plasma diagnostics.* Nuclear Fusion **18**, 647 (1978).

[60] R. Fischer, C. Fuchs, B. Kurzan, W. Suttrop, E. Wolfrum, and A. U. Team. *Integrated data analysis of profile diagnostics at ASDEX Upgrade.* Fusion Science and Technology **58**, 675 (2010).

[61] R. Fischer, A. Burckhart, N. Hicks, B. Kurzan, E. Wolfrum, and A. U. Team. *Multiple diagnostic data analysis of density and temperature profiles in ASDEX Upgrade.* In *Proc. 36th EPS Conf. on Plasma Physics (Sofia, Bulgaria, 2009)*, vol. 33E. Europhysics Conference Abstracts (2009).

[62] V. Dose and W. Von der Linden. *Outlier tolerant parameter estimation.* In *Maximum Entropy and Bayesian Methods Garching, Germany 1998*, pp. 47–56. Springer (1999).

[63] R. Potzel, S .and Dux, H. Müller, A. Scarabosio, M. Wischmeier *et al. Electron density determination in the divertor volume of ASDEX Upgrade via Stark broadening of the Balmer lines.* Plasma Physics and Controlled Fusion **56**, 025010 (2014).

[64] H. Griem. *Principles of Plasma Spectroscopy*, vol. 2. Cambridge University Press (2005).

[65] A. Brissaud and U. Frisch. *Theory of Stark broadening—II exact line profile with model microfield.* Journal of Quantitative Spectroscopy and Radiative Transfer **11**, 1767 (1971).

[66] M. Weinlich. *Elektrostatische Sonden in starken Magnetfeldern.* Phd thesis, Fakultät für Physik, TU München (1995).

[67] D. Bohm, E. Burhop, and H. Massey. *The use of probes for plasma exploration in strong magnetic fields.* Tech. rep. (1948).

[68] G. V. Pereverzev and P. N. Yushmanov. *ASTRA. Automated System for Transport Analysis in a Tokamak.* `http://edoc.mpg.de/display.epl?mode=doc&id=282186&col=33&grp=1311` (2002). IPP Report 5/98.

[69] M. Willensdorfer, E. Fable, E. Wolfrum, L. Aho-Mantila, F. Aumayr, R. Fischer, F. Reimold, F. Ryter *et al. Particle transport analysis of the density build-up after the L-H transition in ASDEX Upgrade.* Nuclear Fusion **53**, 093020 (2013).

[70] B. LaBombard. *KN1D: A 1-D space, 2-D velocity, kinetic transport algorithm for atomic and molecular hydrogen in an ionizing plasma.* Citeseer (2001).